Foundations of VISAR analysis

Daniel H. Dolan

Approved for public release; further dissemination unlimited.

Sandia National Laboratories

Foundations of VISAR analysis

Daniel H. Dolan

Shock and Z-pinch Physics

Sandia National Laboratories

P.O. Box 5800

Albuquerque, NM 87185-1181

dhdolan@sandia.gov

Abstract

The Velocity Interferometer System for Any Reflector (VISAR) is a widely used diagnostic at Sandia National Laboratories. Although the operating principles of the VISAR are well established, recently deployed systems (such as the fast push-pull and air delay VISAR) require more careful consideration, and many common assumptions about VISAR are coming into question. This report presents a comprehensive review of VISAR analysis to address these issues. Detailed treatment of several interferometer configurations is given to identify important aspects of the operation and characterization of VISAR systems. The calculation of velocity from interferometer measurements is also described. The goal is to derive the standard VISAR analysis relationships, indicate when these relationships are valid, and provide alternative methods when the standard analysis fails.

Acknowledgments

Table of Contents

6

List of Figures

List of Tables

CHAPTER 1

Introduction

Velocity measurements play a vital role in dynamic compression research. When combined with mass and momentum conservation, material and wave velocity measurements yield mechanical information for materials under extreme conditions [1]. Velocity is generally easier to measure than other continuum properties (*e.g.,* stress or temperature), and in some case, is the only information obtainable in highly compressed systems.

Numerous optical techniques exist for measuring velocity under extreme conditions. Active shock breakout [2], where changes in the reflected light *intensity* signal the arrival of mechanical waves, is one example; inclined mirror measurements [3], which rely on changes in reflected light *direction*, is another. The most versatile optical velocity measurements are based on changes in the reflected optical *phase*, a generalization of more familiar quantities (such as wavelength). In practice, optical phase cannot be measured directly; instead, an interferometer is used to measure the difference between the optical phase at two different times.

Shock compression experiments using velocity interferometry date back to the 1960's [4], but such measurements were rare until the development of the Velocity Interferometer System for Any Reflector (VISAR) [5]. Since that time, VISAR systems have become a standard velocity diagnostic. Over the years, improvements and modifications to the original VISAR configuration have been made, including the development of multiple channel systems, increased tolerance to incoherent light, and better time resolution [6].

1.1   Overview of a VISAR measurement

The essential components of a VISAR measurement are illustrated in Figure 1.1. Coherent light (typically from a 514.5 or 532 nm laser) is used to illuminate the object of interest. An optical relay directs light toward the object and collects the reflected radiation. Reflected light is sent to an interferometer, producing an output containing the input signal and a time delayed version of the input signal. The output is sensed with fast optical detectors and analyzed to infer the object's motion.

VISAR analysis is comprised of two basic operations: determining the fringe shift and
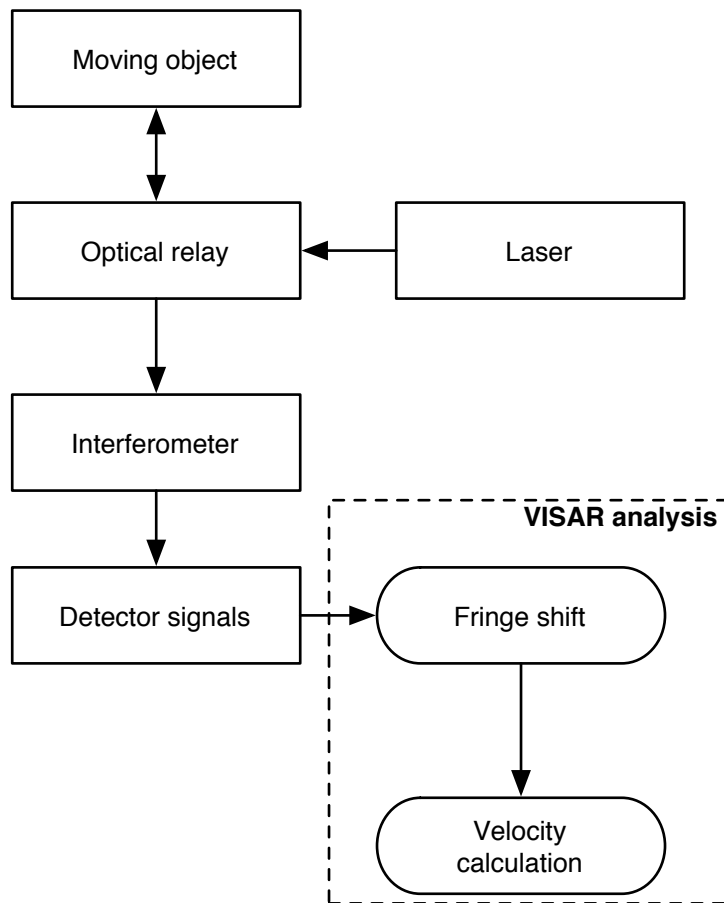
Figure 1.1. Overview of a VISAR measurement.

the velocity calculation. Fringe shift is a normalized measure of how the optical phase difference compares to a reference value. Velocity follows from the fringe shift, and in many applications, is proportional to the fringe shift. Although the two operations are very much related to one another, it is useful to separate them for conceptual clarity.

1.2 Purpose and scope of this work

This report serves three basic purposes. First, the widespread use of VISAR in dynamic compression research has created the need for a comprehensive description of the principles and limitations of this diagnostic. Next, recently deployed systems, such as the fast push-pull VISAR [7] and air delay VISAR [8], challenge traditional assumptions about VISAR and require more careful consideration. Finally, this report precedes the release of a new analysis package, PointVISAR [9], which incorporates much of the theory described here.

Throughout this work, there is an emphasis on the fundamental theory underlying VISAR measurements. At various stages, general results are reduced to standard forms found in most discussions of VISAR. Assumptions and approximations are clearly noted to indicate when the standard forms are valid, and what can be done when they are not. Much of the theory presented here is not new, but has been collected from a variety of published papers and personal discussions as noted in the references.

There are many things that this report does not cover. No attempt is made to follow the history of the VISAR or its use in shock experiments; if this is of interest, the reader is directed to Reference 6. The report focuses exclusively on VISAR measurements of a single point (typically $\ll 1$ mm in diameter) because the vast majority of VISAR measurements are performed at a point or collection of points. For the most part, detector speed limitations are ignored. No attempt has been made to compare the general performance of VISAR with other interferometry methods [10, 11]. This is not meant as a criticism of alternate diagnostics, which may complement VISAR in some situations and supplant it in others. However, VISAR remains the most common velocity diagnostic at Sandia, so such comparisons must be postponed until the alternatives become more established.

1.3 Chapter organization

The organization of this report is intended to match the order of operations in VISAR analysis. Interferometer theory, which forms the bulk of the fringe shift calculation, is presented in Chapter 2. Remaining aspects of the fringe shift calculation and the conversion to velocity are described in Chapter 3. Velocity corrections needed in various situations are discussed in Chapter 4. Characterization and performance assessment of a VISAR system is developed in Chapter 5. An overall summary of VISAR analysis is given in Chapter 6. Appendix A compares the noise performance of two commonly used VISAR configurations.

CHAPTER 2

Interferometer theory

Interferometers are based on wave superposition, which may be constructive or destructive. VISAR systems utilize a specific type of interference, known as division of amplitude [12], where an optical signal is split into distinct paths and later recombined. The classical example of such a system is the Michelson interferometer [13] illustrated in Figure 2.1. Light entering the interferometer is directed along two paths by the beamsplitter (BS) and travels different distances to mirrors M1 and M2. The recombined beams are measured by detector D in the focal plane of lens L. Adjustment of the mirror positions controls the interference of the recombined beams.

The Michelson interferometer provides a conceptual starting point for this discussion. Next, the wide angle Michelson interferometer is described to demonstrate a feasible, though somewhat limited, interferometry system for velocity measurements. Results from the wide angle Michelson interferometer are then applied to the common VISAR configurations (conventional and push-pull) used in dynamic compression research.

2.1   The Michelson interferometer

The basic utility of a Michelson interferometer is its sensitivity to optical phase changes. Optical phase $\phi(t)$ is the time varying quantity that describes oscillations of a coherent electric field E at a particular point in space (for a single light polarization).

$$E = A(t)\cos\phi(t) \tag{2.1}$$

The function $A(t)$ describes field amplitude modulations, which are assumed to be much slower than $\cos\phi(t)$. In this framework, incoherent light may be treated as a superposition of many independent coherent sources, yielding a random optical phase.

For a monochromatic source, the optical phase is linear in time:

$$\phi(t) = \omega_0 t + \phi_0 \tag{2.2}$$

where ω_0 is the radial frequency ($= 2\pi c_0/\lambda_0$) and ϕ_0 is the reference phase at the point of interest.
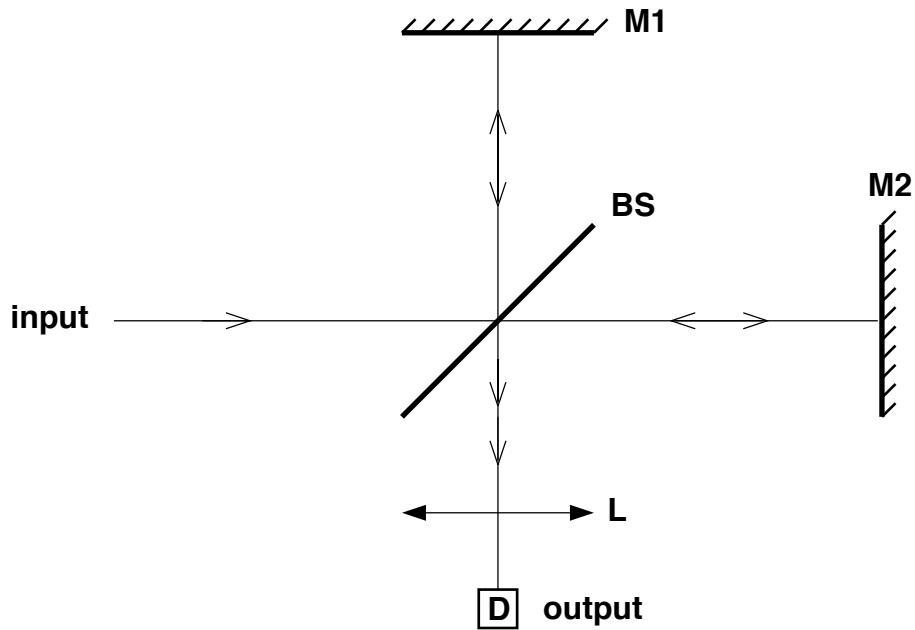
Figure 2.1. The Michelson interferometer.
For clarity, mirrors M1 and M2 are shown at an angle of 90°; in practice, different orientations are used to eliminate multiple reflections and minimize space requirements.

2.1.1 Principles

Suppose that light entering a Michelson interferometer is polarized and collimated, *i.e.* the input electric field is a plane wave with an electric field amplitude $E_0(t)$. In general, the input field is composed of a coherent (subscript "c") and an incoherent (subscript "i") component.

$$E_0(t) = E_c(t) + E_i(t) \tag{2.3}$$

The total electric field at the detector is given by:

$$E(t) = a_1 E_0(t - t_1) + a_2 E_0(t - t_2) \tag{2.4}$$

where a_j represents the coupling and t_j represents the transit time of the j−th leg ($j = 1, 2$). The second path of the Michelson interferometer, which contains mirror M2, is physically longer than the first path by a distance d. The difference in transit time τ between the paths is given by:

$$\tau = t_2 - t_1 = \frac{2d}{c_0} \tag{2.5}$$

where c_0 is the vacuum speed of light.

At visible wavelengths, optical phase oscillates near 10^{15} Hz, substantially faster than any high speed detector ($< 10^9 - 10^{12}$ Hz cutoff). As such, the optical intensity[1] measured by a detector is given by the time average of the total electric field squared [15]:

$$I(t) = \eta \left\langle E^2(t) \right\rangle \tag{2.6}$$

where η is a constant dictated by the electric field units [16]. The intensity of a monochromatic wave is proportional to half the square of its amplitude:

$$\left\langle E^2(t) \right\rangle = \left\langle A^2 \cos^2(\omega_0 t + \delta_0) \right\rangle = \frac{A^2}{2}$$

so the output intensity of a Michelson interferometer is as follows.

$$\begin{aligned}
I(t) &= \eta \left\langle (a_1 E_0(t - t_1) + a_2 E_0(t - t_2))^2 \right\rangle \\
&= \eta \left\langle a_1^2 \left[E_c(t - t_1) + E_i(t - t_1) \right]^2 + a_2^2 \left[E_c(t - t_2) + E_i(t - t_2) \right]^2 \right. \\
&\quad \left. + 2a_1 a_2 \left[E_c(t - t_1) + E_i(t - t_1) \right] \left[E_c(t - t_2) + E_i(t - t_2) \right] \right\rangle
\end{aligned} \tag{2.7}$$

All terms in Equation 2.7 containing a single incoherent factor (at a specific time) average to zero.

$$\begin{aligned}
I(t) &= \eta \left\langle a_1^2 \left[E_c^2(t - t_1) + E_i^2(t - t_1) \right] + a_2^2 \left[E_c^2(t - t_2) + E_i^2(t - t_2) \right] \right. \\
&\quad \left. + 2a_1 a_2 E_c(t - t_1) E_c(t - t_2) \right\rangle
\end{aligned} \tag{2.8}$$

---

[1]The symbol I formally denotes radiant intensity [14], the optical power per unit solid angle. The quantity in Equation 2.6 is actually the irradiance E (optical power per unit area), which is proportional to the Poynting vector [15]. The symbol I is used to prevent confusion between irradiance and electric field.

The first two terms can be expressed in terms of the input intensity.

$$I_0(t) = \eta \left\langle E_0^2(t) \right\rangle = \eta \left\langle E_c^2(t) + E_i^2(t) \right\rangle$$

$$I(t) = a_1^2 \, I_0(t - t_1) + a_2^2 \, I_0(t - t_2) + 2a_1 a_2 \eta \left\langle E_c(t - t_1) E_c(t - t_2) \right\rangle \tag{2.9}$$

The remaining bracketed term can be expanded by assuming that the interferometer input contains a single coherent signal.

$$E_c(t) = A(t) \cos \phi(t)$$

$$\left\langle E_c(t - t_1) E_c(t - t_2) \right\rangle = A(t - t_1) A(t - t_2) \left\langle \cos \phi(t - t_1) \cos \phi(t - t_2) \right\rangle \tag{2.10}$$

The time average can be reduced by recalling that $2\cos A \cos B = \cos(A + B) + \cos(A - B)$. The first term averages to zero: if $\cos \phi(t)$ averages to zero, a similar result would occur for the sum of two phase functions. The second term, however, doesn't necessarily average to zero because the difference between two phases may be a slowly varying function. For compactness, the phase difference will be denoted by the variable $\Phi(t)$.

$$\Phi(t) \equiv \phi(t - t_1) - \phi(t - t_2) \quad (= \omega_0 \tau \text{ for monochromatic input}) \tag{2.11}$$

$$\left\langle E_c(t - t_1) E_c(t - t_2) \right\rangle = \frac{A(t - t_1) A(t - t_2)}{2} \cos \Phi(t) \tag{2.12}$$

The value of $A(t)$ can be expressed in terms of the coherent input intensity I_c.

$$I_c(t) = \eta \left\langle A^2 \cos^2 \phi(t) \right\rangle = \frac{\eta A^2(t)}{2}$$

$$\left\langle E_c(t - t_1) E_c(t - t_2) \right\rangle = \frac{1}{\eta} \sqrt{I_c(t - t_1) I_c(t - t_2)} \cos \Phi(t) \tag{2.13}$$

Combining the results for $\left\langle E_c(t - t_1) E_c(t - t_2) \right\rangle$ with Equation 2.9 yields the complete expression for the output intensity as a function of input intensity and phase difference.

$$I(t) = a_1^2 \, I_0(t - t_1) + a_2^2 \, I_0(t - t_2) + 2a_1 a_2 \sqrt{I_c(t - t_1) I_c(t - t_2)} \cos \Phi(t) \tag{2.14}$$

The output signal $D(t)$ is proportional to the total power striking the detector and the detector responsivity, which is assumed to be constant over the detector's active area and the narrow wavelength range of interest. These proportionality factors can be merged into a new set of coupling constants $\hat{a}_1$ and $\hat{a}_2$.

$$D(t) = \hat{a}_1^2 \, I_0(t - t_1) + \hat{a}_2^2 \, I_0(t - t_2) + 2\hat{a}_1 \hat{a}_2 \sqrt{I_c(t - t_1) I_c(t - t_2)} \cos \Phi(t) \tag{2.15}$$

2.1.2 Limitations

In practice, the input of a Michelson interferometer cannot be perfectly collimated, which means that radiation is distributed over some angular range. To illustrate this point, it is

helpful to think of a Michelson interferometer in terms of the equivalent optical system [15] shown in Figure 2.2. From the detector's point of view, the beamsplitter and mirrors create two virtual images (I1 and I2) of the input. Since each interferometer path is traversed twice in one round trip, the virtual sources are separated by a distance of $2d$.

Collimating lens L transforms light traveling in a particular direction to a point on the detector D. As shown in Figure 2.2, normal rays are imaged at the center of the detector, while rays emitted at an angle θ are imaged to radius r from the center. The mapping of angle to detector location is controlled by the focal length f.

$$r = f\theta \tag{2.16}$$

In most situations, r ($\lesssim 0.5$ mm) is much smaller than f (~ 25 mm), so the relevant angular range is quite small ($\lesssim 1°$).

Light emitted by the virtual sources at a particular angle can be treated as a plane wave passing through that angle; interference at each angle is then conceptually similar to the preceding discussion. For simplicity, consider the input to be entirely coherent and assume that interferometer coupling constants are equal $(a_1 = a_2 = a)$. A spatially uniform intensity I_0 from the source in the direction θ results in an angular intensity $I(\theta)$ at the lens.

$$\begin{aligned} I(\theta) &= 2\hat{a}^2 I_0 \left[1 + \cos \omega_0 \tau(\theta) \right] \\ &= \frac{I_{max}}{2} \left[1 + \cos \omega_0 \tau(\theta) \right] \quad \left(I_{max} = 4\hat{a}^2 I_0 \right) \end{aligned} \tag{2.17}$$

The angular dependence of τ is evident in Figure 2.2 as the path between the virtual sources varies with the angle θ.

$$\tau(\theta) = \frac{2d}{c_0 \cos \theta} \tag{2.18}$$

Combining this result with Equations 2.16–2.17 yields the following intensity distribution.

$$I(r) = \frac{I_{max}}{2} \left[1 + \cos \left(\frac{4\pi d}{\lambda_0} \sec \frac{r}{f} \right) \right] \tag{2.19}$$

This intensity pattern corresponds to a series of circular fringes, also known as Haidinger fringes or fringes of equal inclination [17], in the detector plane. If one mirror is tilted with respect the other, the virtual images are no longer parallel and the interference pattern changes to parallel fringes, also known as Fizeau fringes or fringes of equal thickness [17]. Michelson interferometers are generally constructed to eliminate Fizeau fringes, allowing the circular fringe pattern to be seen.

The intensity at the central point of the detector $(r = 0)$ is given by:

$$I(r = 0) = \frac{I_{max}}{2} \left[1 + \cos \frac{4\pi d}{\lambda_0} \right] \tag{2.20}$$

so the center is brightest when d is an even multiple of $\lambda_0/8$ and darkest when d is an odd multiple of $\lambda_0/8$. However, the detector signal is proportional to an integral over the
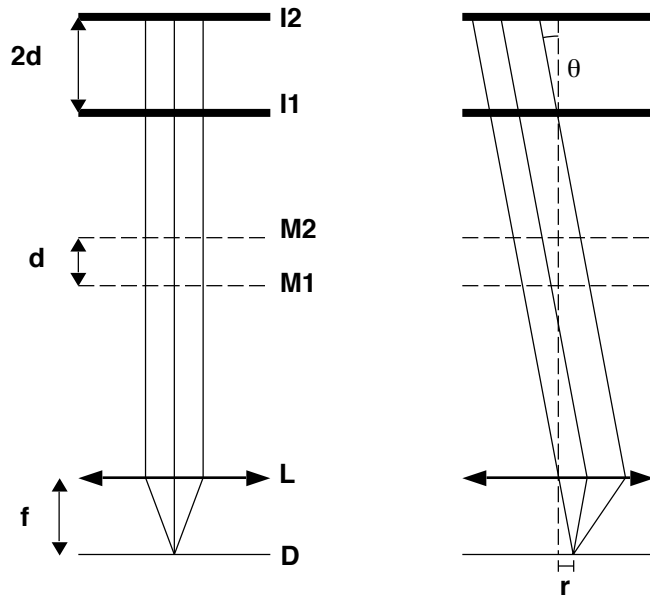
Figure 2.2. Equivalent optical system for the Michelson interferometer
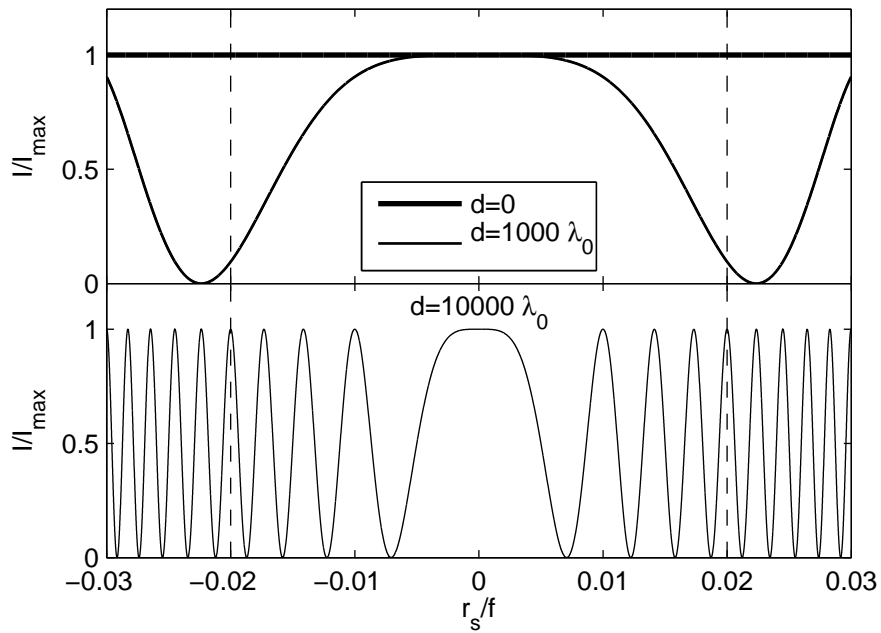
Figure 2.3. Output intensity profile for a Michelson interferometer.

active area, not just the central intensity. The extent to which intensity variations affect the measurement can be characterized by the spot size r_s, defined here as the distance from a central bright spot to the first intensity minimum.

$$\frac{r_s}{f} \approx \arccos\left(\frac{4\pi d/\lambda_0}{1+4\pi d/\lambda_0}\right) \approx \begin{cases} \dfrac{\pi}{2} & (d \ll \lambda_0) \\ \sqrt{\dfrac{\lambda_0}{2d}} & (d \gg \lambda_0) \end{cases} \tag{2.21}$$

For small mirror separations, the interferometer spot size is comparable to f, leading to uniform detector illumination. Large mirror separations, however, lead to small spot sizes and appreciable intensity variations.

To illustrate the significance of intensity variations, consider an interferometer coupled to a 1 mm diameter detector by a 25 mm focal length lens ($r/f \leq 0.02$). Figure 2.3 shows the intensity distribution on the output detector for several values of d/λ. Even at moderate mirror separations ($d = 1000 \lambda_0$), the detector intensity is obviously not constant. The problem is even more severe at $d = 10000 \lambda_0$, where the central spot lies entirely inside the detector along with additional intensity cycles. Since the outer cycles carry a significant fraction of the total power striking the detector, the fact that the central spot is bright only weakly affects the output signal. The distinction between constructive and destructive interference is thus quite subtle, and eventually disappears at very large mirror separations.

In principle, intensity distribution issues could be mitigated with the use of a sufficiently small detector. However, this solution leads to low signal levels as little of the input power can be collected by the detector. An alternate solution is to operate the interferometer at $d = 0$, which produces a flat intensity field. While this may seem an attractive solution, it would eliminate the relative delay between the combined signals, rendering the system useless for measuring phase difference. Instead, one must use a modified configuration or carefully collimate light entering the system [8].

2.2 The wide angle Michelson interferometer

The shortcomings of the Michelson interferometer can be overcome by creating a non-zero mirror separation that has zero virtual separation. This is achieved by placing an uncompensated dielectric slab or etalon in one leg of the interferometer, creating a wide angle Michelson interferometer (WAMI) [18] as shown in Figure 2.4. The purpose of the etalon is to create a virtual mirror image M2' that is closer to the beam splitter than the actual mirror M2, yielding a uniform detector illumination. Since the interferometer legs have different physical lengths, there remains a relative time delay (and thus interference) between the recombined light signals. This time delay is a function of the size and optical properties of the etalon, and is derived in Section 5.1. For now, it will be assumed that the delay time is known.
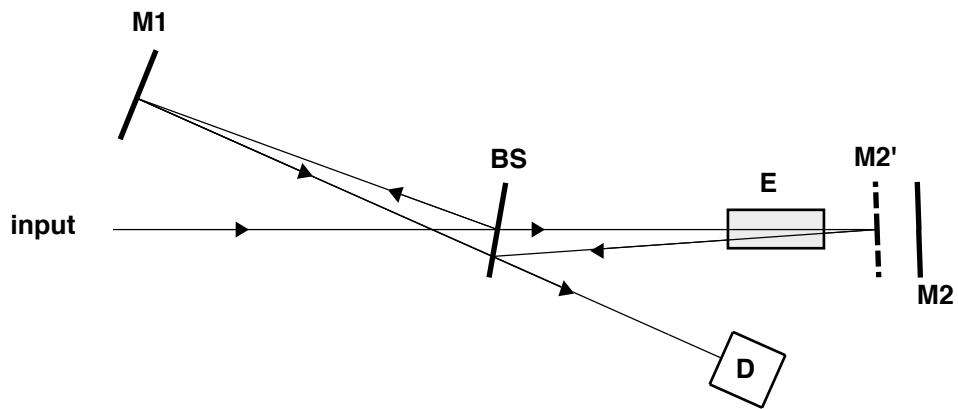
Figure 2.4. The wide angle Michelson interferometer (WAMI)
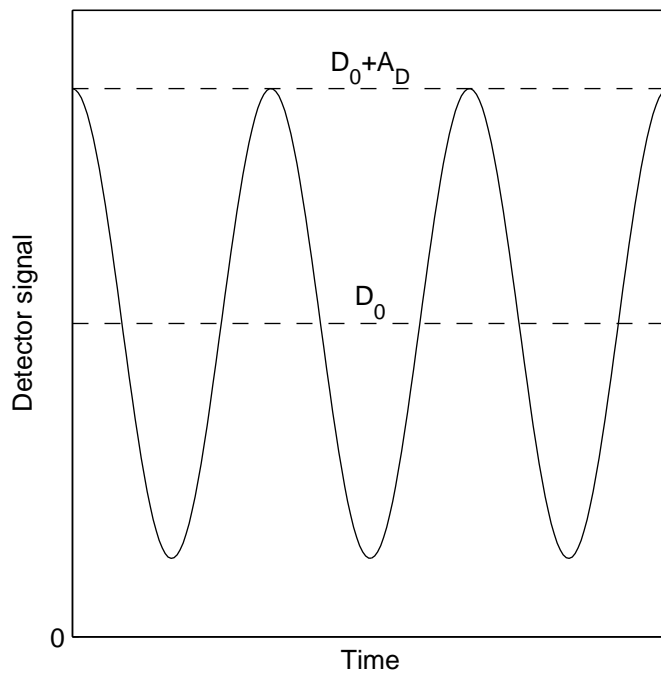
Figure 2.5. WAMI output signals.

2.2.1 Principles

From the discussion in Section 2.1, the detector output from a WAMI can be expressed as follows.

$$D(t) = \hat{a}_1^2 \, I_0(t - t_1) + \hat{a}_2^2 \, I_0(t - t_2) + 2\hat{a}_1\hat{a}_2 \sqrt{I_c(t - t_1)I_c(t - t_2)} \cos \Phi(t) \qquad (2.22)$$

The phase difference $\Phi(t)$ describes the difference in phase between light passing through each leg of the interferometer.

$$\Phi(t) = \phi(t - t_1) - \phi(t - t_1 - \tau) \qquad (2.23)$$

In situations where the input is completely coherent ($I_0 = I_c$) with a slowly varying amplitude, the detector output can be reduced to a simpler form.

$$D(t) = I_0(t) \left[\hat{a}_1^2 + \hat{a}_2^2 + 2\hat{a}_1\hat{a}_2 \cos \Phi(t) \right] \qquad (2.24)$$

To illustrate the sensitivity of a WAMI to phase changes, suppose that the input intensity is constant. For convenience, the value of I_0 will be combined with the scaling factors as follows.

$$D_0 \equiv I_0 \left(\hat{a}_1^2 + \hat{a}_2^2 \right) \qquad\qquad A_D \equiv 2I_0 \, \hat{a}_1\hat{a}_2$$
$$D(t) = D_0 + A_D \cos \Phi(t) \qquad (2.25)$$

The detector output is thus a sinusoidal function of Φ with an offset D_0 and an amplitude A_D. If the phase difference increases linearly in time, the detector signal for a WAMI would appear as shown in Figure 2.5. When the input is monochromatic, the value of $\Phi(t)$ is simply $\omega_0\tau$, so variations in $D(t)$ correspond to changes in the product of input frequency and the time delay. Once the time delay has been determined, a WAMI is capable of sensing minute frequency changes, a capability that can be tied to the Doppler shift of light reflected from a moving target.

The oscillation magnitude in a WAMI cannot exceed the signal offset. Quantitatively, this constraint can be formulated in terms of the interferometer scaling factors.

$$A_D \leq D_0 \leftrightarrow 2\hat{a}_1\hat{a}_2 \leq \hat{a}_1^2 + \hat{a}_2^2 \qquad (2.26)$$

The values of $\hat{a}_i$ dictate the system contrast, a quantity that describes the ability of the interferometer to distinguish constructive and destructive interference. The numerical definition of contrast [15], also called fringe visibility, is given by:

$$C = \frac{I_{max} - I_{min}}{I_{max} + I_{min}} = \frac{D_{max} - D_{min}}{D_{max} + D_{min}} \qquad (2.27)$$

where I_{max} is the maximum intensity (corresponding to constructive interference) and I_{min} is the minimum intensity (corresponding to destructive interference). From this definition,

contrast is always between zero and unity. For the WAMI, contrast can be expressed as follows.

$$D_{max} = D_0 + A_D \qquad\qquad D_{min} = D_0 - A_D$$

$$C = \frac{A_D}{D_0} \qquad\qquad (2.28)$$

Maximum contrast occurs when the oscillation magnitude equals the signal offset, which can only be achieved when $\hat{a}_1 = \hat{a}_2$.

2.2.2 Limitations

Although the WAMI is capable of measuring phase changes, there are a number of practical difficulties for this configuration. These problems fall into two general categories: input sensitivity and phase uncertainty.

Input sensitivity describes the WAMI's inability to separate variations of input intensity from phase changes. When the input intensity is time dependent or contains incoherent light, these variations are carried in the detector output along with optical phase changes. As such, it can be difficult to interpret data from a WAMI unless optical phase is the only time varying quantity.

Phase uncertainty occurs in the WAMI because of the cosine function in Equation 2.25. The periodic nature of this function means that a particular value of D corresponds to an infinite number of values of Φ, each differing by an integer multiple of 2π. Furthermore, the symmetry of the cosine function at $\Phi = 0$ and $\Phi = \pi$ creates sign ambiguities that obscure whether Φ is increasing or decreasing. Determining the phase angle near the symmetry points, where light intensity is at a minimum or maximum, is also imprecise because of the flatness of the detector signal.

2.3 The conventional VISAR

The conventional VISAR (Velocity Interferometer System for Any Reflector) [5] is a robust system that builds upon the strengths of the WAMI. Shown schematically in Figure 2.6, the conventional VISAR is essentially two WAMI systems that operate on different polarizations of the input. Light entering the interferometer is intentionally unpolarized, resulting in two output signals obtained with a polarizing beamsplitter (PBS) and a pair of detectors (D1 and D2). The two polarizations are phase shifted with respect to one another through the use of a 1/8 wave plate (WP) in one leg of the interferometer. Finally, a beam intensity monitor (BIM) is located at the input of the interferometer for tracking changes in the input intensity.
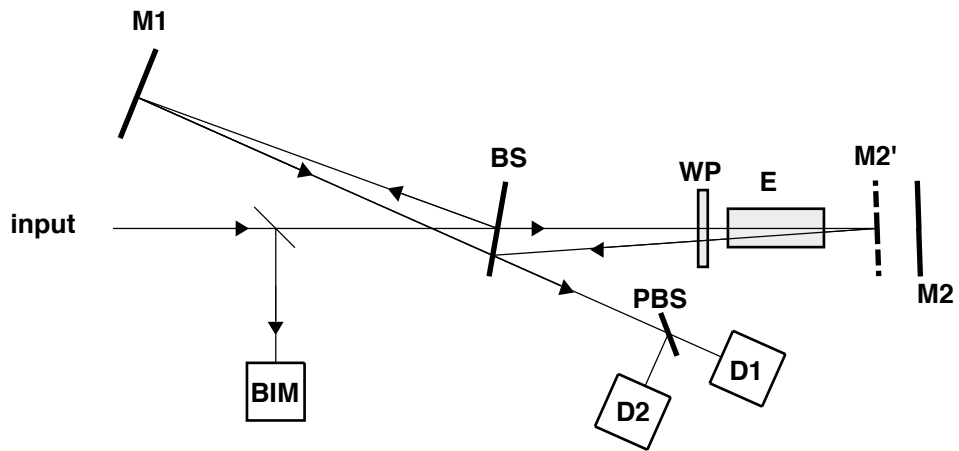
Figure 2.6. The conventional VISAR.
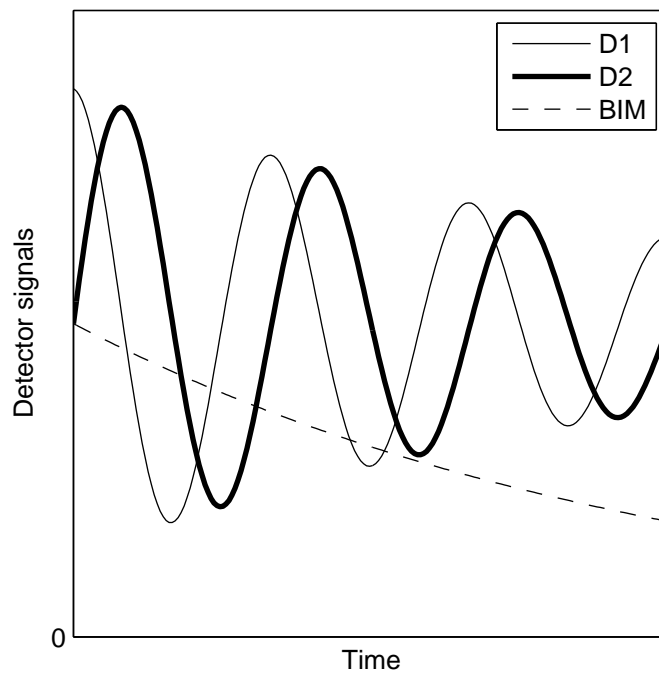
Figure 2.7. Conventional VISAR detector output signals.

2.3.1 Principles

The output of one VISAR detector is similar to a WAMI system with the addition of an extra subscript to indicate which polarization is being measured.

$$D_1(t) = \hat{a}_{11}^2 \, I_0(t-t_1) + \hat{a}_{21}^2 \, I_0(t-t_2) + 2\hat{a}_{11}\hat{a}_{21} \sqrt{I_c(t-t_1)I_c(t-t_2)} \cos \Phi(t) \qquad (2.29)$$

In this notation, $\hat{a}_{ij}$ refers to the coupling factor for light of polarization j passing through leg i. The output of the second detector has a similar form:

$$D_2(t) = \hat{a}_{12}^2 \, I_0(t-t_1) + \hat{a}_{22}^2 \, I_0(t-t_2) + 2\hat{a}_{12}\hat{a}_{22} \sqrt{I_c(t-t_1)I_c(t-t_2)} \cos \Phi_2(t) \qquad (2.30)$$

where Φ_2 is a phase difference function that accounts for the round trip passage through the $1/8$ wave plate. The wave plate time delays both polarizations by a certain amount, generating a small correction to the value of τ, but of critical importance is the delay difference between polarizations. This difference can be associated with a relative phase delay β.

$$\Phi_2(t) = [\phi(t-t_2) - \beta] - \phi(t-t_1) = \Phi(t) - \beta \qquad (2.31)$$

The value of β is controlled by rotating the $1/8$ wave plate about its axis; since light passes through the plate twice, the phase shift ranges from zero to one quarter of a wave. When $\beta = \pi/2$, the two detector signals are said to be in perfect quadrature. It is convenient to express β in terms of a quadrature error ε, which describes how far off the system is from perfect quadrature.

$$\Phi_2(t) = \Phi(t) - \pi/2 - \varepsilon \qquad (2.32)$$

Combining this definition with the above expression for D_2 converts the cosine factor to a sine.

$$D_2(t) = \hat{a}_{12}^2 \, I_0(t-t_1) + \hat{a}_{22}^2 \, I_0(t-t_2) + 2\hat{a}_{12}\hat{a}_{22} \sqrt{I_c(t-t_1)I_c(t-t_2)} \sin\left(\Phi(t) - \varepsilon\right) \quad (2.33)$$

Figure 2.7 shows a conceptual example of how the D_1, D_2 and BIM signals would appear for a measurement of steadily increasing $\Phi(t)$ and decreasing input intensity.

The BIM is not exposed to any interference, and is thus directly proportional to total input intensity.

$$D_{BIM}(t) = \hat{a}_3^2 \, I_0(t-t_3) \qquad (2.34)$$

The time shift t_3 reflects the fact that light striking the BIM travels along a different path than that reaching detectors D1 and D2; the constant $\hat{a}_3^2$ originates from coupling factors associated with that path. If it is assumed that the input intensity varies slowly with respect to the time scales t_1, t_2, and t_3, then the factors $I_0(t-t_i)$ $(i = 1, 2, 3)$ can be replaced by $I_0(t)$. Under such circumstances, it becomes advantageous to normalize the signals D_1 and D_2 with respect to the BIM:

$$D_x \equiv \frac{D_1(t)}{D_{BIM}(t)} = \underbrace{\bar{a}_{11}^2 + \bar{a}_{21}^2}_{x_0} + \underbrace{2\bar{a}_{11}\bar{a}_{21} \frac{I_c(t)}{I_0(t)} \cos \Phi(t)}_{A_x(t)} \qquad (2.35)$$

$$D_y \equiv \frac{D_2(t)}{D_{BIM}(t)} = \underbrace{\bar{a}_{12}^2 + \bar{a}_{22}^2}_{y_0} + \underbrace{2\bar{a}_{12}\bar{a}_{22} \frac{I_c(t)}{I_0(t)} \sin\left(\Phi(t) - \varepsilon\right)}_{A_y(t)} \qquad (2.36)$$

24

where the barred variables indicate the ratio of an interferometer coupling factor to the BIM coupling factor (*e.g.,* $\bar{a}_{11}^2 = \hat{a}_{11}^2/\hat{a}_3^2$).

Each normalized signal is composed of two contributions—a constant offset and sinusoidal function (with possibly a time dependent amplitude)—that parametrically define a family of ellipses. For fixed values of I_c/I_0, the output of the interferometer lies along a single ellipse as shown in Figure 2.8. Ideally, the ellipse is a circle centered about the point $(1,1)$ with an amplitude of unity, but in general $I_c \leq I_0$, so the amplitude is less than or equal to the offset and the system contrast is less than or equal to unity.[2]. An additional complication is imperfect quadrature ($\varepsilon \neq 0$), which leads to non-circular ellipses.

Conversion from a point (D_x, D_y) on the ellipse to the angle Φ is found by taking the ratio of the sinusoidal terms in Equations 2.35 and 2.36.

$$\cos\Phi(t) = \frac{D_x(t) - x_0}{A_x(t)}$$

$$\sin(\Phi(t) - \varepsilon) = \frac{D_y(t) - y_0}{A_y(t)} = \sin\Phi(t)\cos\varepsilon - \cos\Phi(t)\sin\varepsilon$$

$$\tan\Phi(t) = \tan\varepsilon + \frac{D_y(t) - y_0}{D_x(t) - x_0}\frac{A_x(t)}{A_y(t)}\sec\varepsilon \tag{2.37}$$

Note that $A_x(t)/A_y(t)$ is independent of input power fluctuations.

2.3.2 Limitations

Unlike the WAMI, the conventional VISAR is insensitive to variations of the input intensity, a benefit gained through BIM normalization. After normalization, the center of a conventional ellipse is essentially fixed; the ellipse size may vary with changes of the input intensity ratio, but such effects cancel out in the calculation of phase difference. For purely coherent input, normalized VISAR signals trace out a single ellipse; changes in the coherent/incoherent ratio move the data across a family ellipse of the same shape.

Since the calculation of phase difference in a conventional VISAR involves a tangent rather than a cosine function, many of the limitations of the WAMI are removed. By *careful* evaluation of the inverse tangent, it is possible to remove the sign ambiguity from Φ and determine if this quantity is increasing or decreasing. Also, the use of quadrature signals avoids the issues near maxima and minima—since these signals cannot simultaneously be zero, the accuracy in calculating Φ is dramatically improved. The conventional VISAR retains the 2π phase ambiguity present in WAMI systems, but this ambiguity is not insurmountable (Section 5.4.1).

---

[2]Strictly speaking, there are two contrast values in a conventional VISAR, but they are typically assumed to be identical [19].
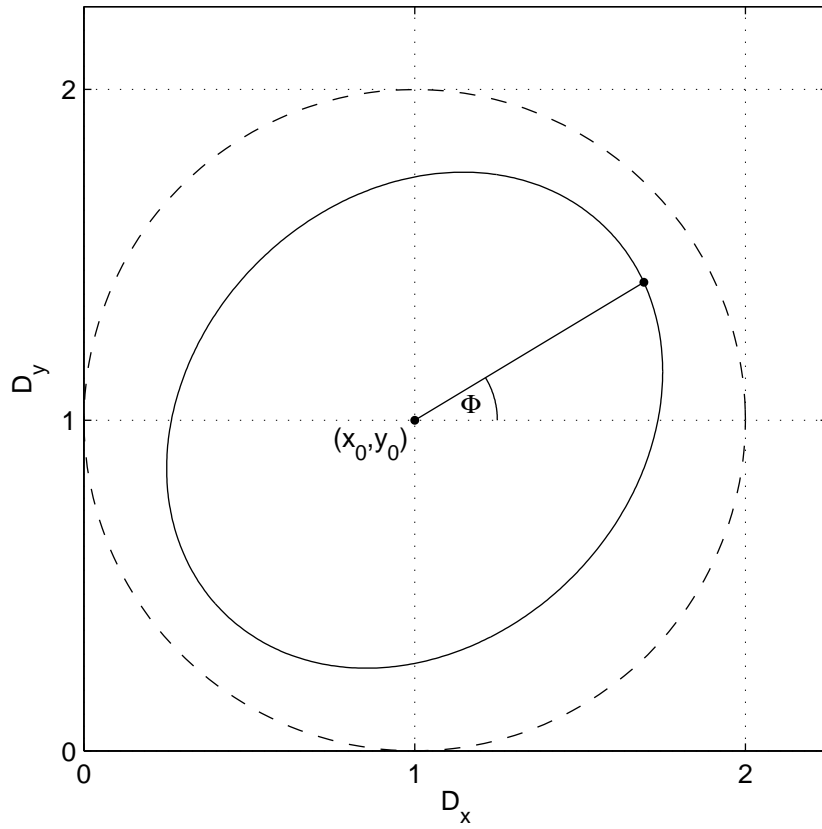
Figure 2.8. Examples of an imperfect (solid line) and perfect (dashed line) ellipse for a conventional VISAR.

2.4 The push-pull VISAR

A modification to the conventional VISAR was proposed by Hemsing [20] to improve the efficiency of light usage. In a conventional VISAR, half of the light entering the system does not reach the detectors, but is lost by reflection/transmission to the opposite side of the primary beamsplitter. This light can be used to drive a second set of detectors as shown in Figure 2.9, creating two conventional VISARs (one on each side of the beamsplitter) and thus four optical signals. Subtraction between the appropriate signal pairs creates what is known as a push-pull VISAR. Traditionally, subtraction is performed by electronic differential amplifiers prior to data acquisition. For maximum time resolution, all four detector signals can be acquired separately, an approach becoming more common in current VISAR systems [7].

2.4.1 Principles

For notational simplicity, it is assumed here that the second pair of detectors in a push-pull VISAR are located precisely the same distance from the beamsplitter as the first pair; if this is not true, a minor timing correction may be needed to align the two signal pairs. Also, the polarizing beamsplitters are assumed to be aligned in a similar fashion so that the same optical polarization is measured by detectors D1A/D1B and D2A/D2B. The second pair of detectors in a push-pull VISAR operate in nearly the same fashion as the first pair with the exception of a negative sign for one coupling constant. This change results from different recombination of beams at the beamsplitter (*e.g.,* light from leg 1 is reflected rather than transmitted). The results from the previous section can thus be applied to a push-pull system with specific coupling constants for each signal.

$$
\begin{aligned}
D_{1A}(t) = \hat{a}_{11}^2 \, I_0(t-t_1) + \hat{a}_{21}^2 \, I_0(t-t_2) \\
+ 2\hat{a}_{11}\hat{a}_{21}\sqrt{I_c(t-t_1)I_c(t-t_2)}\cos\Phi(t) \quad (2.38)
\end{aligned}
$$

$$
\begin{aligned}
D_{2A}(t) = \hat{a}_{12}^2 \, I_0(t-t_1) + \hat{a}_{22}^2 \, I_0(t-t_2) \\
+ 2\hat{a}_{12}\hat{a}_{22}\sqrt{I_c(t-t_1)I_c(t-t_2)}\sin\left(\Phi(t)-\varepsilon\right) \quad (2.39)
\end{aligned}
$$

$$
\begin{aligned}
D_{1B}(t) = \hat{b}_{11}^2 \, I_0(t-t_1) + \hat{b}_{21}^2 \, I_0(t-t_2) \\
- 2\hat{b}_{11}\hat{b}_{21}\sqrt{I_c(t-t_1)I_c(t-t_2)}\cos\Phi(t) \quad (2.40)
\end{aligned}
$$

$$
\begin{aligned}
D_{2B}(t) = \hat{b}_{12}^2 \, I_0(t-t_1) + \hat{b}_{22}^2 \, I_0(t-t_2) \\
- 2\hat{b}_{12}\hat{b}_{22}\sqrt{I_c(t-t_1)I_c(t-t_2)}\sin\left(\Phi(t)-\varepsilon\right) \quad (2.41)
\end{aligned}
$$

In many cases, no BIM is available in push-pull VISAR systems—either no measurement of input intensity is made, or if it is, the measurement is shared across multiple VISAR channels. Hence, BIM normalization is not typically performed in a push-pull VISAR. Figure 2.10 shows an example of how the four detector signals of a push-pull VISAR would appear for steadily increasing $\Phi(t)$ and decreasing input intensity.

As in a conventional VISAR, it is convenient to assume that the input intensity variations
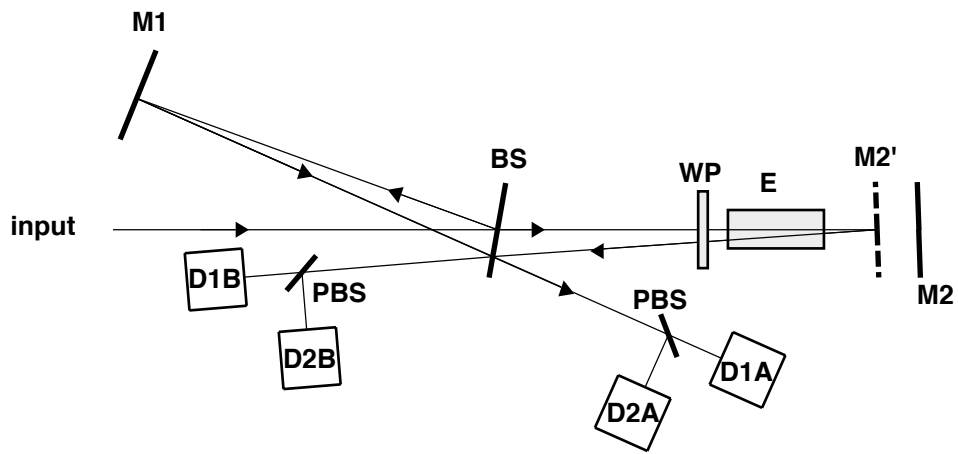
Figure 2.9. The push-pull VISAR.
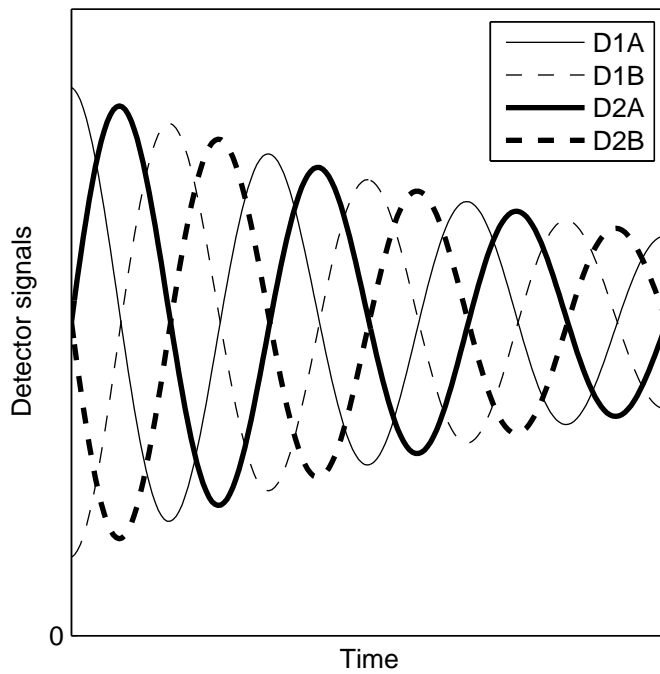
Figure 2.10. Push-pull VISAR signals.

28

of a push-pull VISAR are slow compared to the interferometer transit times.

$$D_{1A}(t) = \left(\hat{a}_{11}^2 + \hat{a}_{21}^2\right) I_0(t) + 2\hat{a}_{11}\hat{a}_{21} I_c(t) \cos \Phi(t) \tag{2.42}$$

$$D_{2A}(t) = \left(\hat{a}_{12}^2 + \hat{a}_{22}^2\right) I_0(t) + 2\hat{a}_{12}\hat{a}_{22} I_c(t) \sin \left(\Phi(t) - \varepsilon\right) \tag{2.43}$$

$$D_{1B}(t) = \left(\hat{b}_{11}^2 + \hat{b}_{21}^2\right) I_0(t) - 2\hat{b}_{11}\hat{b}_{21} I_c(t) \cos \Phi(t) \tag{2.44}$$

$$D_{2B}(t) = \left(\hat{b}_{12}^2 + \hat{b}_{22}^2\right) I_0(t) - 2\hat{b}_{12}\hat{b}_{22} I_c(t) \sin \left(\Phi(t) - \varepsilon\right) \tag{2.45}$$

Pairwise subtraction of the signals from each side of the beamsplitter results in two signals:

$$D_x(t) \equiv \eta_{1A} D_{1A}(t) - \eta_{1B} D_{1B}(t) \tag{2.46}$$
$$= \underbrace{\left[\eta_{1A}\left(\hat{a}_{11}^2 + \hat{a}_{21}^2\right) - \eta_{1B}\left(\hat{b}_{11}^2 + \hat{b}_{21}^2\right)\right] I_0(t)}_{x_0(t)} + \underbrace{2\left[\eta_{1A}\hat{a}_{11}\hat{a}_{21} + \eta_{1B}\hat{b}_{11}\hat{b}_{21}\right] I_c(t)}_{A_x(t)} \cos \Phi(t)$$

$$D_y(t) \equiv \eta_{2A} D_{2A}(t) - \eta_{2B} D_{2B}(t) \tag{2.47}$$
$$= \underbrace{\left[\eta_{2A}\left(\hat{a}_{12}^2 + \hat{a}_{22}^2\right) - \eta_{2B}\left(\hat{b}_{12}^2 + \hat{b}_{22}^2\right)\right] I_0(t)}_{y_0(t)} + \underbrace{2\left[\eta_{2A}\hat{a}_{12}\hat{a}_{22} + \eta_{2B}\hat{b}_{12}\hat{b}_{22}\right] I_c(t)}_{A_y(t)}$$

where η is a scaling factor for each signal, which can be controlled by physical means (*e.g.,* increasing the gain for a particular detector) or numerically. As in the case of a conventional VISAR, these signals parametrically describe an ellipse, although now the ellipse center is a function of the total input intensity, and can change during the measurement. To avoid this complication, push-pull VISAR signals must be properly scaled to fix the ellipse center at the origin (Section 5.2.2).

$$D_x(t) = A_x(t) \cos \Phi(t) \tag{2.48}$$
$$D_y(t) = A_y(t) \sin \left(\Phi(t) - \varepsilon\right) \tag{2.49}$$

Note that D_x and D_y are symmetric about zero, which by Equation 2.27 corresponds to infinite signal contrast. Since this is meaningless, one typically refers to the dynamic contrast defined in Section 5.3.1.

Following the same logic leading to Equation 2.37, the phase difference is related to the reduced push-pull data signals through a tangent function.

$$\tan \Phi(t) = \tan \varepsilon + \frac{y(t)}{x(t)} \frac{A_x(t)}{A_y(t)} \sec \varepsilon \tag{2.50}$$

Aside from the fact that the center of the ellipse is located at the origin, the analysis of a push-pull VISAR is very similar to the analysis of a conventional VISAR. The overall size of a push-pull ellipse is proportional to the coherent intensity, rather than the coherent intensity fraction, but such variations do not affect the calculation of phase difference as the ratio $A_x(t)/A_y(t)$ is independent of $I_c(t)$.

2.4.2 Limitations

The push-pull VISAR shares many of the benefits and shortcomings of the conventional VISAR. With the correct signal balancing, a push-pull VISAR is insensitive to variations

in the input intensity and incoherent light. Phase uncertainty is reduced by the use of quadrature, although the 2π ambiguity remains and must be dealt with just as in a conventional VISAR. The push-pull VISAR has largely supplanted conventional VISAR in dynamic compression research, so it is worthwhile to consider the relative benefits of each system. The relative advantages of each system will be considered in three areas: low light sensitivity, analysis simplicity, and tolerance to rapid intensity changes.

For measurements with low coherent intensity, the push-pull configuration has some advantages over a conventional VISAR. Certainly the push-pull system makes the most efficient use of input intensity, although there is no more than $2-4$ times more light than in a conventional VISAR. This additional light gives a push-pull VISAR approximately 40% better noise performance (Appendix A) over a similar conventional VISAR. The push-pull configuration also has an advantage when large amounts of incoherent light are present; if pairwise subtraction is performed prior to signal acquisition, a larger dynamic range to the coherent signal of interest. However, the gains of a push-pull VISAR come with certain costs. In addition to the extra equipment needs and alignment, a push-pull VISAR *must* be properly balanced in order to achieve the same accuracy as a conventional VISAR. Hence, one should not assume that measurements made with a push-pull VISAR are intrinsically superior.

From an analysis perspective, a push-pull VISAR is easier to deal with than a conventional VISAR. Conventional VISAR analysis requires an ellipse fit to determine the ellipse center, a step that may be unnecessary (though certainly recommended) for a well configured push-pull system. There is also an intuitive advantage to a push-pull VISAR because the ellipse radius is a function of coherent light only—changes in incoherent intensity do not cause the VISAR ellipse to contract as for a conventional VISAR.

When input intensity changes on time scales comparable to τ, the analysis described above will yield a transient contrast loss. A revised analysis is straightforward for the conventional VISAR configuration when an accurate BIM signal is present and all detectors are precisely cross-timed.

$$D_1(t) = \frac{\hat{a}_{11}^2}{\hat{a}_3^2} D_{BIM}(t + t_3 - t_1) + \frac{\hat{a}_{21}^2}{\hat{a}_3^2} D_{BIM}(t + t_3 - t_2)$$
$$+ 2\hat{a}_{11}\hat{a}_{21}\sqrt{I_c(t-t_1)I_c(t-t_2)}\cos\Phi(t) \qquad (2.51)$$

$$D_2(t) = \frac{\hat{a}_{12}^2}{\hat{a}_3^2} D_{BIM}(t + t_3 - t_3) + \frac{\hat{a}_{22}^2}{\hat{a}_3^2} D_{BIM}(t + t_3 - t_2))$$
$$+ 2\hat{a}_{12}\hat{a}_{22}\sqrt{I_c(t-t_1)I_c(t-t_2)}\sin(\Phi(t) - \varepsilon) \qquad (2.52)$$

By isolating terms containing $I_c(t)$ and taking a ratio, it should be possible to extract phase difference information from the three data signals. Rapid variations are harder to deal with in a push-pull VISAR because there is often no direct measure of the input intensity. During a rapid intensity variation, a push-pull VISAR becomes unbalanced and the center drifts

away from the origin. To demonstrate this, consider just one optical polarization.

$$x_0(t) = \eta_{1A} \left[\hat{a}_{11}^2 I_0(t-t_1) + \hat{a}_{21}^2 I_0(t-t_2) \right] - \eta_{1B} \left[\hat{b}_{11}^2 I_0(t-t_1) + \hat{b}_{21}^2 I_0(t-t_2) \right]$$
$$= \left[\eta_{1A} \hat{a}_{11}^2 - \eta_{1B} \hat{b}_{11}^2 \right] I_0(t-t_1) + \left[\eta_{1A} \hat{a}_{21}^2 - \eta_{1B} \hat{b}_{21}^2 \right] I_0(t-t_2) \qquad (2.53)$$

Except in certain special cases, it is impossible to balance a push-pull for arbitrary input intensity.

CHAPTER 3

Optical velocimetry

Optical phase based velocimetry relies on the relativistic Doppler effect [21]. When a moving object is illuminated with light of wavelength λ_0, the reflected wavelength is given by:

$$\frac{\lambda}{\lambda_0} = \frac{1 - v/c_0}{1 + v/c_0} \approx 1 - 2\,v/c_0 \tag{3.1}$$

where v is the object velocity and c_0 is the vacuum speed of light; the approximation follows from the fact that v/c_0 is typically less than 0.001. Hence, measurements of reflected wavelength (or more precisely, the reflected optical phase) can be used to track object motion.

The theory behind optical velocimetry is developed here in three stages. First, the forward problem is considered to show how known object motion can be used to predict the resulting changes in optical phase. Next, the forward problem is inverted to demonstrate a process for extracting velocity from measured optical phase changes. The general result is then reduced to a simpler form, denoted here as the VISAR approximation, that relates the velocity of an object directly to an interferometer measurement.

3.1 The forward problem

Suppose that an object of interest is a reflector[1] of negligible thickness located at position $x(t)$ at time t. At an arbitrary reference position x_r, chosen to be always to the right of the object, monochromatic light is emitted at time t_A as shown in Figure 3.1. This light reaches the object at time t_B, is reflected, and returns to the reference plane at time t_C.

Throughout this discussion, it will be assumed that the object velocity is always substantially smaller than the speed of light. As such, terms containing powers of $(v/c_0)^2$ or higher will be neglected. Although the Doppler shift is often derived with assumption of constant object velocity, this is not necessary when dealing with optical phase, which is frame invariant [16]. Hence, the general result derived here does not place any limits upon the

---

[1] Apart from practical details (*e.g.,* optical relay design and efficiency), the reflector may be specular or diffuse. This is one advantage of the VISAR over a Michelson interferometer [22] for open beam optical relays.

time A

object

emission

reference plane

time B

reflection

time C

detection
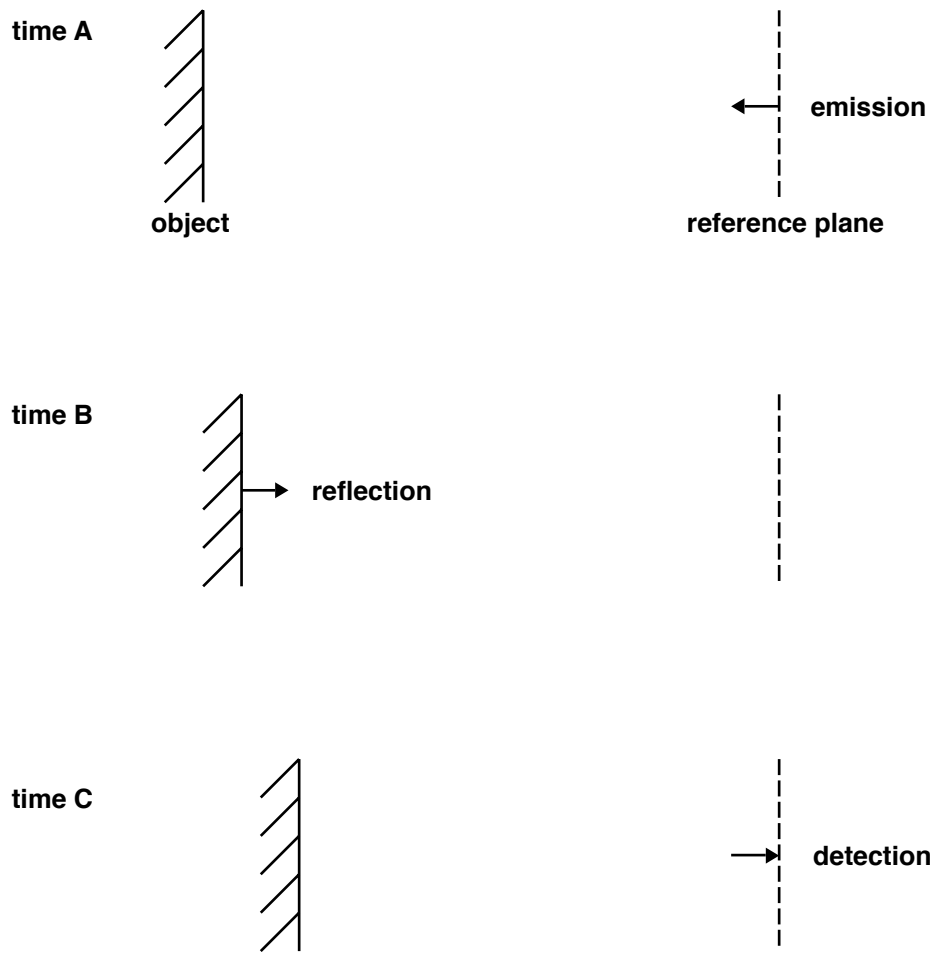
Figure 3.1. Light transit in an optical velocity measurement.

magnitude of acceleration, although it is assumed that extremely large accelerations exist for only brief intervals so that $v \ll c_0$.

3.1.1 Reflected optical phase

The output optical phase at time t_C is equivalent to the input phase at time t_A [23], aside from a possible phase delay δ_m from the reflection (assumed to be constant). For monochromatic input, this equivalence can be expressed as follows.

$$\phi(t_C) = \phi_{in}(t_A) - \delta_m$$
$$= \omega_0 t_A + \phi_0 - \delta_m \tag{3.2}$$

Events at t_A and t_C are separated from the reflection at t_B by a duration T:

$$t_A = t_B - T \qquad\qquad t_C = t_B + T$$
$$T = \frac{x_r - x(t_B)}{c_0} \tag{3.3}$$

so the output phase is related to the object position at an earlier time.

$$\phi(t_C) = \omega_0(t_C - 2T) + \phi_0 - \delta_m$$
$$= \omega_0 \left[t_C - \frac{2}{c_0}(x_r - x(t_C - T)) \right] + \phi_0 - \delta_m \tag{3.4}$$

A VISAR does not measure optical phase, but rather the phase difference (Chapter 2):

$$\Phi(t) = \phi(t - t_1) - \phi(t - t_2) \tag{3.5}$$

where t_1 and t_2 are the interferometer transit times. Using Equation 3.4, phase difference can be expressed as:

$$\Phi(t) = \frac{2\omega_0}{c_0} \left[\frac{c_0}{2}(t_2 - t_1) + x(t - t_1 - T_1) - x(t - t_2 - T_2) \right]$$
$$= \frac{4\pi}{\lambda_0} \left[\frac{c_0}{2}(t_2 - t_1) + x(t - t_1 - T_1) - x(t - t_2 - T_2) \right] \tag{3.6}$$

where T_i represents the transit time of light from position $x(t - t_i - T_i)$ to the reference position, now located at the entrance plane of the interferometer.

The value of T_i can be determined from Equation 3.3.

$$T_i = \frac{x_r - x(t - t_i - T_i)}{c_0} \tag{3.7}$$

The actual transit times are rarely needed as changes in T_i are bounded by the maximum position change during an experiment of duration t_{exp}.

$$\Delta T_i \leq \frac{\Delta x}{c_0} \leq \frac{v_{max}}{c_0} t_{exp} \tag{3.8}$$

35

Variations in T_i are generally small compared to diagnostic limitations. Throughout this work, it is assumed that T_i can be treated as a constant; for higher timing precision, iterative evaluation of Equation 3.7 must be performed.

The interferometer transit times are related by the interferometer delay τ:

$$t_2 = t_1 + \tau \tag{3.9}$$

where t_1 is usually constant. Ideally τ is also constant, but this quantity can vary with velocity if the interferometer contains dispersive components (Section 5.1.2).

$$\tau = \tau_0 \left(1 + 2\delta \frac{v(t - t_1 - \tau - T)}{c_0} \right) \tag{3.10}$$

The dispersion free delay is given by τ_0, the dispersion magnitude by δ, and the object velocity by $v(t)$. The Taylor series expansion of $x(t - \tau)$ differs from $x(t - \tau_0)$ only by terms of order $(v/c_0)^2$ or higher; also, dispersive variations in τ are of opposite sign from the changes in the transit time T and partially cancel.[2] Thus, it is reasonable to replace $x(t - \tau)$ with $x(t - \tau_0)$ and $v(t - \tau)$ with $v(t - \tau_0)$ in Equation 3.6.

$$\Phi(t) = \frac{4\pi}{\lambda_0} \left[\frac{c_0 \tau_0}{2} \left(1 + 2\delta \frac{v(t - t_1 - \tau_0 - T)}{c_0} \right) + x(t - t_1 - T) \right.$$
$$\left. - x(t - t_1 - \tau_0 - T) \right] \tag{3.11}$$

For notational compactness, a new quantity x' will be used to eliminate constant time shifts.

$$x'(t) \equiv x(t - t_1 - T) \tag{3.12}$$

$$\Phi(t) = \frac{4\pi}{\lambda_0} \left[\frac{c_0 \tau_0}{2} \left(1 + 2\delta \frac{v'(t - \tau_0)}{c_0} \right) + x'(t) - x(t - \tau_0) \right] \tag{3.13}$$

In later chapters, the primes will be omitted, but they are retained here to remind the reader of the fundamental time shift between object motion and the measured signals.

Given a known motion history, Equation 3.13 describes phase difference at an operating wavelength λ_0 and delay time τ_0. At any given time, phase difference is dictated by the current position as well as the position at a time τ_0 earlier. Forward analysis can also be used when object motion history is expressed by a known function with a finite number of adjustable parameters; these parameters would be adjusted to optimally match the measured phase difference. However, such analysis is not generally used in velocimetry measurements because it is relatively slow and does not guarantee a unique solution.

---

[2]Motion towards the interferometer corresponds to an increase of τ (for $\delta > 0$) but a decrease in T; similar logic applies for motion away from the interferometer

3.1.2 Physical interpretation

To develop some physical intuition, suppose that dispersion is negligible in a particular VISAR measurement.

$$\Phi(t) = \frac{4\pi}{\lambda_0} \left[\frac{c_0 \tau_0}{2} + x'(t) - x'(t - \tau) \right] \tag{3.14}$$

The first term is a constant that is independent of motion. The primary concern of this discussion is value of $x'(t) - x'(t - \tau)$.

When an object is at rest, Equation 3.14 indicates that the measured phase difference will be a constant. Furthermore, measurements at constant velocity yield a different constant phase.

$$\Phi(t) \sim x'(t) - x'(t - \tau) = v\tau \quad \text{(constant velocity)} \tag{3.15}$$

A particular velocity corresponds to a certain phase difference, so it follows that changes in velocity are linked to changes in phase difference. Since the phase difference scales with product of velocity and interferometer delay, it is possible to configure a VISAR to optimally track a particular velocity range (*e.g.,* choosing a large delay time for small velocities).

The qualitative behavior of a VISAR make it a "velocity interferometer". If the object under study formed one leg of a Michelson interferometer [22], phase difference would change with displacement, making it a "displacement interferometer". Velocity interferometers are better suited for the study of fast moving objects as rapidly changing phase differences from a displacement interferometer may be difficult to track. However, the term "velocity interferometer" may be misleading as VISAR data can be analyzed in terms of velocity or displacement. Aside from numerical issues discussed later on, the two analysis approaches are identical.

3.2 The inverse problem

Velocimetry measurements are the inverse of the above discussion—given a measured phase difference, the position [24–26] is determined; velocity may then derived by numerical differentiation. Conceptually, there is little difficulty in inverting Equation 3.13.

$$x'(t) = x'(t - \tau_0) + \frac{\lambda_0}{4\pi} \Phi(t) - \frac{c_0 \tau_0}{2} \left(1 + 2\delta \frac{v'(t - \tau_0)}{c_0} \right) \tag{3.16}$$

The inverse problem is iterative because the result at time t depends on conditions at an earlier time $t - \tau_0$. Before delving into the details of the iteration, one must first specify an initial condition to begin the calculation.

3.2.1 Initial conditions

Suppose that an object moves at a fixed velocity v_i for $t \leq t_i$. The object's position at t_i may then be written as follows.

$$x'(t_i) = x'(t_i - \tau_0) + \frac{\lambda_0}{4\pi}\Phi(t_i) - \frac{c_0\tau_0}{2}\left(1 + 2\delta\frac{v'(t_i - \tau_0)}{c_0}\right) = x'(t_i - \tau_0) + v_i\tau_0$$

$$v_i'\tau_0 = \frac{\lambda_0}{4\pi}\Phi(t_i) - \frac{c_0\tau_0}{2}\left(1 + 2\delta\frac{v_i'}{c_0}\right) \tag{3.17}$$

This expression can be used to write the initial phase difference in terms of the initial velocity.

$$\Phi(t_i) = \frac{4\pi\tau_0}{\lambda_0}\left[\frac{c_0}{2} + (1 + \delta)v_i'\right] \tag{3.18}$$

Note that the value of $\Phi(t_i)$ may drift due to the thermal/mechanical variations in the interferometer. Such variations are general slow compared to duration of a single measurement, but may be significant between measurements. Hence, the numerical value of $\Phi(t_i)$ is always calculated from the initial quadrature signals in a VISAR measurement, not from Equation 3.18.

By convention [27], interferometer measurements are expressed in terms of a fringe shift $F(t)$, which describes the change in phase difference at a particular time from the initial phase difference (normalized by a complete phase revolution).

$$F(t) \equiv \frac{\Phi(t) - \Phi(t_i)}{2\pi} \tag{3.19}$$

$$\Phi(t) = \Phi(t_i) + 2\pi F(t) = \frac{4\pi\tau_0}{\lambda_0}\left[\frac{c_0}{2} + (1 + \delta)v_i'\right] + 2\pi F(t)$$

Equation 3.16 can be rewritten in terms of the fringe shift.

$$x'(t) = x'(t - \tau_0) + (1 + \delta)\tau_0 v_i' + \frac{\lambda_0}{2}F(t) - \delta\tau_0 v'(t - \tau_0) \tag{3.20}$$

To begin using Equation 3.20, the initial condition position $x'(t_i)$ must be specified. Since $x'(t)$ is usually differentiated to yield $v'(t)$, the value of $x'(t_i)$ is arbitrary and typically set to zero.

3.2.2 Iterative analysis

Inverse analysis relies on iterative analysis of the fringe shift data. Analysis begins at $t = t_i$, and proceeds throughout the fringe shift record. At a particular time t, the current position is determined from the current fringe shift, the position at $t - \tau_0$, and the velocity at $t - \tau_0$. Interpolation may be required if the time base of $F(t)$ is not compatible with τ_0, but in principle, the calculation is straightforward.

Although inverse analysis provides a potentially exact description of the object's motion, there are practical difficulties that limit the utility of this method.

1. Signal noise

   Noise is a problem for numerical differentiation, which is needed to convert position to velocity and to evaluate $v'(t - \tau_0)$ in dispersive systems. Hence, velocity noise will be substantially worse than signal noise.

2. Missing data

   Intervals of missing fringe shift data, such as when contrast is completely lost (Section 5.3), present problems for inverse analysis. If the interval is very short, position change may be negligible, so it might be permissible to skip over the missing data [26]. Extended periods of missing data, however, would be more difficult to handle.

Thus, it is often impractical to apply inverse analysis to a VISAR measurement.

3.3   The VISAR approximation

It is often is desirable to calculate velocity directly from the measured fringe shift. This can be done using an approximate analysis for time scales much larger than τ_0. Such treatment is known as the VISAR approximation, an approach used in most data reduction schemes.

3.3.1   Derivation

Suppose that the position $x(t)$ is an analytic function [28], so that the function at time t can be represented in terms of a Taylor series expansion from $t - \tau_0$.

$$x(t) = x(t - \tau_0) + v'(t - \tau_0)\tau_0 + a'(t - \tau_0)\frac{\tau_0^2}{2!} + \frac{da'(t - \tau_0)}{dt}\frac{\tau_0^3}{3!} + \cdots \tag{3.21}$$

Here $a'(t)$ is the objects's acceleration. Substitution of this expansion into Equation 3.20 eliminates the term $x(t - \tau_0)$.

$$v'(t - \tau_0)\tau_0 + a'(t - \tau_0)\frac{\tau_0^2}{2!} + \frac{da'(t - \tau_0)}{dt}\frac{\tau_0^3}{3!} + \cdots = (1 + \delta)\tau_0 v_i' + \frac{\lambda_0}{2}F(t) - \delta\tau_0 v(t - \tau_0) \tag{3.22}$$

This leads to the following expression for $v'(t - \tau_0)$:

$$v'(t - \tau_0) = v_i' + \underbrace{\frac{\lambda_0}{2(1 + \delta)\tau_0}}_{K}F(t) - a'(t - \tau_0)\frac{\tau_0}{2!(1 + \delta)}$$

$$- \frac{da'(t - \tau_0)}{dt}\frac{\tau_0^2}{3!(1 + \delta)} - \cdots \tag{3.23}$$

where K is the fringe constant or VPF (Velocity Per Fringe) of the interferometer.

Truncation of Equation 3.23 yields the most basic form of the VISAR approximation.

$$v'(t - \tau_0) \approx v'_i + KF(t) + \mathcal{O}(\tau_0) \tag{3.24}$$

The reasoning behind this truncation is that τ_0 is typically a small number, so terms that scale with τ_0 are negligible, especially in comparison with $1/\tau_0$. In many cases, the time shift is omitted, leading to another form of the VISAR approximation.

$$v'(t) \approx v'_i + KF(t) + \mathcal{O}(\tau_0) \tag{3.25}$$

Higher accuracy is possible if one considers a Taylor series expansion of velocity from time $t - \tau_0$ to $t - \gamma\tau_0$, where γ is a constant.

$$v'(t - \gamma\tau_0) = v'(t - \tau_0) + a'(t - \tau_0)(1 - \gamma)\tau_0 + \frac{da'(t - \tau_0)}{dt}\frac{(1 - \gamma)^2\tau_0^2}{2!} + \cdots \tag{3.26}$$

Combining this expansion with Equation 3.23 yields the following series.

$$\begin{aligned}
v'(t - \gamma\tau_0) = v'_i + KF(t) + &\left(1 - \gamma - \frac{1}{2!(1 + \delta)}\right)a'(t - \tau_0)\tau_0 \\
&+ \left(\frac{(1 - \gamma)^2}{2!} - \frac{1}{3!(1 + \delta)}\right)\frac{da'(t - \tau_0)}{dt}\tau_0^2 + \cdots
\end{aligned} \tag{3.27}$$

Choosing $\gamma = (1/2 + \delta)/(1 + \delta) \approx (1 + \delta)/2$ forces the acceleration term to zero, so a truncation of the series has an error of order τ^2.

$$v'(t - \gamma\tau_0) \approx v_i + KF(t) + \mathcal{O}(\tau_0^2) \tag{3.28}$$

This is the standard form of the VISAR approximation [27], although in practice Equation 3.25 is commonly used in data reduction. Examples in the next subsection demonstrate when the distinction between approximations is important.

The VISAR approximation has many practical advantages over inverse analysis. Foremost among these is the fact that velocity is directly proportional to fringe shift. This simple relation avoids iteration and makes the calculation far more robust. Noise amplification is no longer an issue as signal noise translates directly to velocity noise. Missing data is also not an issue in the VISAR approximation—picking up the calculation after momentary or extended periods of contrast loss is trivial.

The disadvantage of the VISAR approximation lies in its inability to track motion changes on time scales comparable to τ_0. This is not an issue when the interferometer delay is shorter than the diagnostic time resolution, but is becoming an issue in modern VISAR systems [8]. Truncation of the Taylor series leading to Equation 3.28 assumes that next term in the series is substantially smaller than the VISAR resolution (Section 5.4.2).

$$\begin{aligned}
\frac{da'(t - \tau_0)}{dt}\frac{\tau_0^2}{24} &\ll K\,(\delta F) \lesssim \frac{K}{100 - 200} \quad \text{(no dispersion)} \\
\frac{da'(t - \tau_0)}{dt} &\ll \frac{\lambda_0}{10\,\tau_0^3}
\end{aligned} \tag{3.29}$$

For sufficiently small values of da'/dt, the VISAR approximation is reliable. Although it is tempting to generate higher accuracy by considering $v(t - \tau/4)$ (*i.e.* Richardson extrapolation [29]), refinements achieved by this process are lost when the motion history is not analytic.

3.3.2 Examples

To illustrate the performance of the VISAR approximation at different time scales, consider an ideal case where an object moves with a linearly increasing velocity that terminates at a maximum value v_m at time t_r.

$$v'(t) = \begin{cases} 0 & t \leq 0 \\ v_m \dfrac{t}{t_r} & 0 < t \leq_r \\ v_m & t > t_r \end{cases} \tag{3.30}$$

Suppose that this motion is tracked by a dispersion free VISAR with delay time τ_0 and fringe constant K. To eliminate the use of specific values for K and v_m, the problem can be formulated in terms of normalized quantities:

$$\tilde{v} = \frac{v}{v_m} \qquad\qquad \tilde{x} = \frac{x}{v_m \tau_0}$$

$$\tilde{t} = \frac{t}{\tau_0} \qquad\qquad \tilde{F} = \frac{KF}{v_m} \qquad\qquad g = \frac{t_r}{\tau_0}$$

which lead to normalized expressions for the inverse analysis and VISAR approximation.

$$\tilde{x}(\tilde{t}) = \tilde{x}(\tilde{t} - 1) + \tilde{F}(\tilde{t}) \tag{3.31}$$

$$\tilde{v}(\tilde{t} - 1/2) \approx \tilde{F}(\tilde{t}) \tag{3.32}$$

The normalized motion history is given by the following expressions.

$$\tilde{v}(\tilde{t}) = \begin{cases} 0 & \tilde{t} \leq 0 \\ \tilde{t}/g & 0 < \tilde{t} \leq g \\ 1 & \tilde{t} > g \end{cases} \tag{3.33}$$

For this specified velocity, the displacement may be determined analytically:

$$\tilde{x}(\tilde{t}) = \begin{cases} 0 & \tilde{t} \leq 0 \\ \tilde{t}^2/2g & 0 < \tilde{t} \leq g \\ \tilde{t} - g/2 & \tilde{t} > g \end{cases} \tag{3.34}$$

and used with Equation 3.31 to determine the resulting fringe shift. The calculated fringe shift may be then be inserted into Equation 3.32 to determine velocity given by the VISAR approximation.

When the rise time is substantially slower than the interferometer delay, as shown in Figure 3.2(a) for $t_r = 10\ \tau_0$, the standard VISAR approximation (shifted by $\tau_0/2$) is a very good
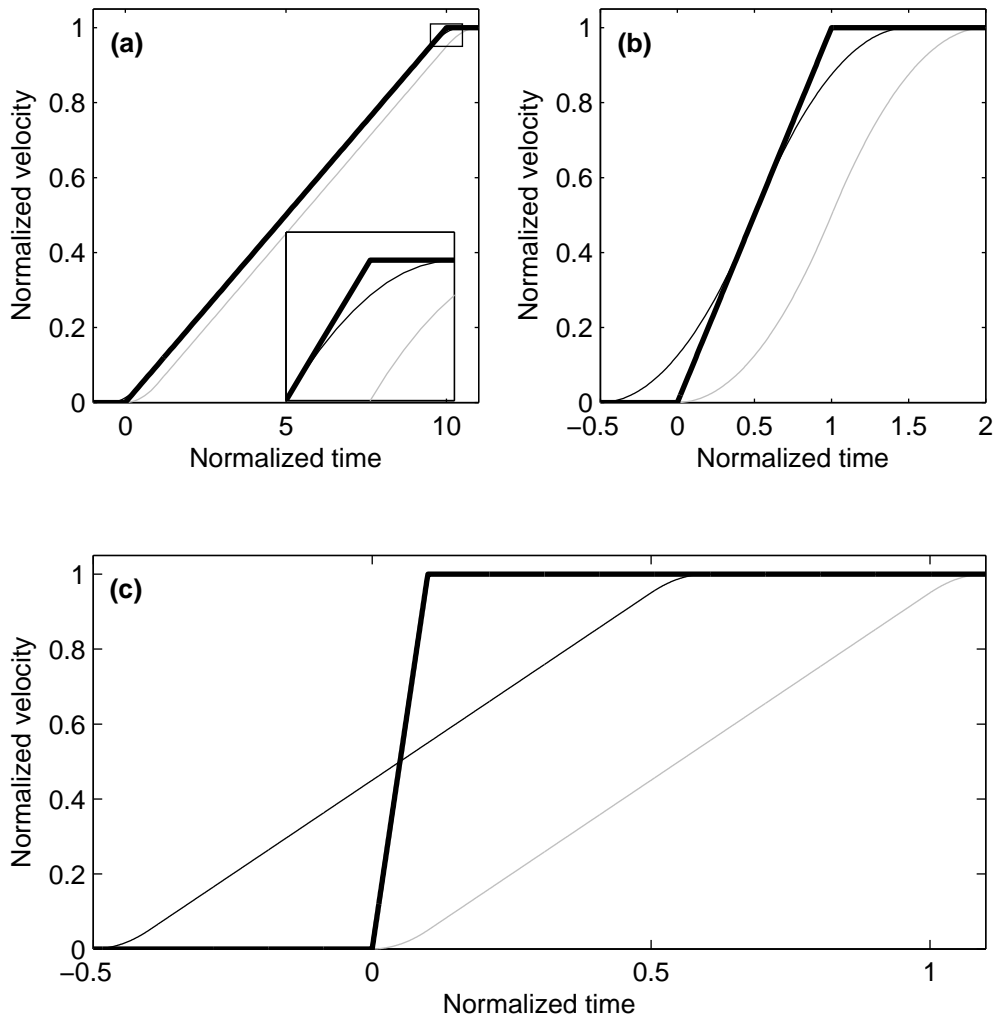
Figure 3.2. VISAR approximation examples.
(a) Slow velocity rise ($t_r = 10\,\tau_0$)
(b) Moderate velocity rise ($t_r = \tau_0$)
(c) Fast velocity rise ($t_r = \tau_0/10$)
Thin black lines show the standard VISAR approximation (shifted
by $\tau_0/2$), while thin gray lines show the unshifted approximation.
Heavy lines indicate the specified velocity histories.

42

match to the actual velocity. The unshifted form of the approximation lies to the right of the input history but has a similar shape; the remaining form of the approximation, where velocity is time shifted by τ_0, would lie to the left of the input history by the same amount (not shown). When τ_0 is smaller than the measurement time resolution, the difference between the different forms of the approximation can be neglected. However, if precise timing is required (*e.g.,* traversal time measurements), it may be important to use the more accurate version of the VISAR approximation. Otherwise, all three forms of the approximation are largely interchangeable.

As the velocity rise time approaches the interferometer delay time, differences between the actual and calculated velocity begin to appear. The critical case $t_r = \tau_0$ is shown in Figure 3.2(b) to illustrate this point. The midpoint of the VISAR approximation crosses the midpoint of the input history, and at this intersection the slopes are equal.[3] However, there are significant deviations during the initial and final portions of the ramp. For rise times faster than the interferometer delay, the VISAR approximation is a poor representation of the true velocity history. Figure 3.2(c) demonstrates this for the case $t_r = \tau_0/10$. Once again, the VISAR approximation crosses the original history at the midpoint, but that is the extent of their agreement. The slope of the VISAR approximation is substantially different than the original history, and the approximation indicates considerable velocity prior to actual motion.

For situations where the VISAR approximation does not work well, velocity can be calculated using inverse analysis. In the absence of noise, inverse analysis reproduces the specified velocity history within numerical precision. In real measurements, the fringe signal is a combination of actual motion and random fluctuations (*e.g.,* detector noise).

$$\tilde{F}(\tilde{t}) = \tilde{F}_{input}(\tilde{t}) + A\sigma(t) \tag{3.35}$$

Here A represents the noise amplitude and $\sigma(t)$ is a random function with a mean value of zero and variance of unity. Combining the forward calculation (Equation 3.33) with this random function produces a noisy fringe shift, which can be used in the inverse analysis to calculate the position history. This result can then be numerically differentiated for a meaningful comparison of the inverse analysis and input history.

Based on the examples shown in Figure 3.2, there is little point in applying inverse analysis to situations where $t_r \gg \tau_0$ as the VISAR approximation does an excellent job with little effort. To illustrate when the inverse analysis might outperform the VISAR approximation, consider the case $t_r = \tau_0$ with a relatively low noise amplitude (0.1%). Several examples of this case are shown in Figure 3.3(a-c). In plot (a), velocity is calculated from a central finite difference method [29]:

$$v(t) = \frac{x(t+t_s) - x(t-t_s)}{2t_s} \tag{3.36}$$

where t_s is the time interval between data points ($t_s = \tau_0/10$ in this example). Inverse analysis provides a reasonable reconstruction of the input history, with minor deviations

---

[3]This agreement results from the fact the VISAR approximation is accurate to τ_0^2. It is large values of jerk (da/dt)—such as the velocity ramp corners—that cause problems, not the acceleration itself.
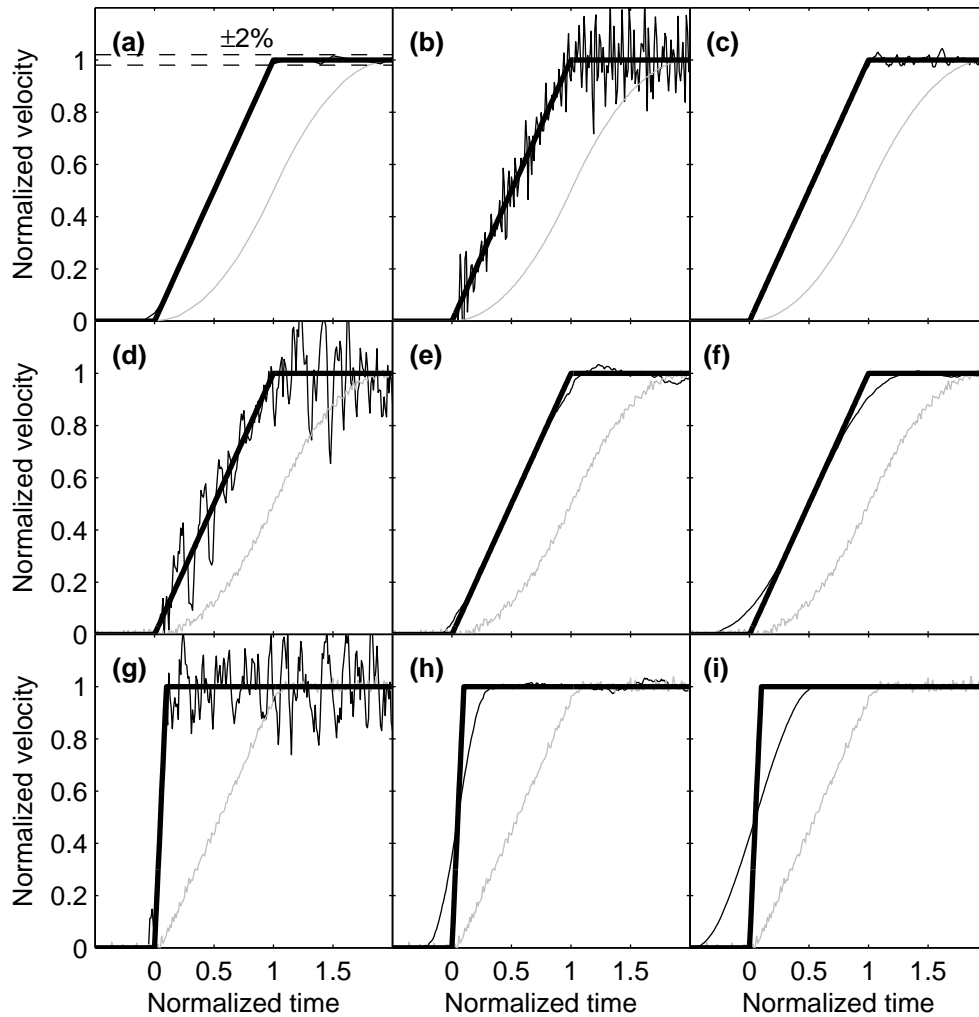
Figure 3.3. Inverse analysis examples.
(a-c) Moderate rise times ($t_r = \tau_0$) and low noise ($A = 0.1\%$)
(d-f) Moderate rise times ($t_r = \tau_0$) and moderate noise ($A = 1\%$)
(g-i) Fast rise times ($t_r = \tau_0/10$) and moderate noise ($A = 1\%$)
Thin black lines show the inverse analysis for a given input history
(heavy black lines) and noise level. Thin gray lines indicate the
unshifted VISAR approximation, which is proportional to fringe
shift, for comparison.

at the beginning and ending of the ramp and some oscillations in the steady state. These oscillations are of order 1-2%, and represent a considerable $(10-20\times)$ amplification of the fringe shift noise. This shortcoming of numerical differentiation is a fundamental concern in any inverse analysis of VISAR data.

The difficulties in performing an inverse analysis are shown more dramatically in Figure 3.3(b). In this case, the sampling interval is decreased from $\tau_0/10$ to $\tau_0/100$ with the same rise time and noise levels as Figure 3.3(a). This change in the sampling rate corresponds to substantially larger steady state noise ($\approx 20\%$) because the finite difference algorithm is sensitive to small variations in neighboring sample points (similar effects can be seen in Ref. 26). One solution for this problem is to perform the derivative over time scales larger than t_s, reducing the effect of point to point noise in the derivative calculation. A convenient way of implementing a derivative time scale is to perform a series of polynomial fits[4] at each point of the calculated displacement:

$$x_{fit}(t) = \sum_{i=1}^{N} a_i(t)\, t^{i-1} \qquad (3.37)$$

where $a_i(t)$ is determined by a least squares fit of $x(t)$ over the range $t - t_d/2 \leq t \leq t + t_d/2$. In addition to smoothing, the use of local polynomial fitting provides an analytic representation of the velocity.

$$v = \frac{dx_{fit}}{dt} = \sum_{i=2}^{N} a_i(t)(i-1)\, t^{i-2} \qquad (3.38)$$

The refined derivative, shown in Figure 3.3(c), is substantially better than Equation 3.36 at dealing with noise. In fact, the refined derivative works even better at higher sampling rates (for fixed values of t_d), although there are practical limits as to how small t_s can be made.

To illustrate the process of selecting a proper value of t_d, consider a moderately noisy signal ($A = 1\%$) as shown in Figure 3.3(d-f); apart from larger noise level, the input history for these plots is identical to Figure 3.3(c). In Figure 3.3(d), a small derivative time ($t_d = \tau_0/10$) is used to allow filtering over approximately ten points (recall that the sampling interval is $\tau_0/100$). Although the calculated velocity follows the general path of the input history, the noisy result ($\approx 20\%$) is hardly a worthwhile gain over the VISAR approximation. Larger derivative time scales, such as $t_d = \tau_0/2$ (Figure 3.3(e)), lead to more reasonable results, but it is imperative that t_d not be too large. In Figure 3.3(f), the derivative time is set equal to τ_0, yielding a result that is quite similar to the VISAR approximation. Similar results can be obtained for faster velocity changes as shown in Figure 3.3(g-i), where a velocity history for $t_r = \tau_0/10$ ($A = 1\%$ and $t_s = \tau_0/100$) is analyzed with derivative times of $\tau_0/10$, $\tau_0/5$, and τ_0 respectively (1% noise levels and $\tau_0/100$ sampling).

The tradeoff between accurate rise times and smoothness is clear: by making t_d large, the results are typically smooth but have a slower rise time. The goal would be to choose t_d

---

[4]This process is similar to a Savitsky-Golay filter [30], but can be implemented in a different fashion to avoid redundant calculations. Linear fits were used to yield the results shown in Figure 3.3.

such that it is no smaller than it needs to be. Obviously, this discussion uses an advantage unavailable in most experiments—the input history is already known—but there are constraints for choosing a reasonable rise time. For a linear velocity ramp (Equation 3.33), the fringe shift rise time equals the sum of the true rise time and the interferometer delay, so an estimate of t_r can be made by subtracting τ_0 from the measured rise time of $F(t)$. Further refinement is possible by performing the calculation for different values of t_d to determine the maximum value that does not substantially broaden the velocity ramp. In general, the time scales in a calculation should obey the following rules.

$$t_s \ll t_d \leq t_r \lesssim \tau_0 \tag{3.39}$$

There are limits on how well ultrafast velocity changes can be detected, even with inverse analysis. Very fast events (*e.g.,* $\tau/100$) correspond to only minor differences between the measured rise time and τ_0, and at some point such differences will be indistinguishable. The precise limit depends upon the detection/acquisition system, but roughly speaking, changes faster than $\tau_0/100$ would be difficult (if not impossible) to extract.

CHAPTER 4
Velocity corrections

In the preceding chapter, it was assumed a VISAR system measures the actual velocity of interest. However, a VISAR is only sensitive to changes in optical phase difference, and different types of motion can yield the same phase difference. Apparent velocity, denoted here with a "$*$" superscript, is the result obtained from the VISAR approximation (Equation 3.28) or the more general inverse analysis (Equation 3.20). With knowledge of the measurement configuration, it is possible to correct the VISAR result and obtain the true object velocity. Note that the distinction between apparent and true velocity is not unique to the VISAR, but applies to any optical phase measurement.

Recall that reflected optical phase is equivalent to the input optical phase at an earlier time (Section 3.1.1):

$$\phi(t) = \phi_0(t - 2T^*) + \delta_m \tag{4.1}$$

were T^* is the apparent transit time between the object and a fixed reference plane. Measurements where illumination and/or reflection is not normal the object's motion, or when light must pass through an optical window, may have a different transit time but yield the same optical phase:

$$\phi(t) = \phi_0(t - T_1 - T_2) + \delta_m \tag{4.2}$$

where T_1 is the transit time from the input plane to the object and T_2 is the transit time from the object to the output plane. Apparent and true motion can be related to one another by equating the two expressions for optical phase, which implies that the total transit times must be the same.

$$T^* = \frac{T_1 + T_2}{2} \tag{4.3}$$

This chapter derives two important classes of velocity correction. First, the problem of non-normal incidence and reflection is described. Next, corrections originating from optical windows are treated.

4.1   Angular illumination and reflection

The optical relay in a velocity measurements rarely matches the ideal configuration (Figure 3.1), where all light paths are parallel to the object's motion. Non-normal illumination

and reflection usually lead to minor differences between the apparent and true velocity, but there are situations where the correction is important. At the very least, the correction provides an estimate of the limiting velocity precision. For large angles, the apparent velocity correction can reveal both longitudinal and transverse motion.

4.1.1 General problem

Consider the reflection geometry shown in Figure 4.1. At an arbitrary time t, a small area element of a reflective surface, shown here as a point, is located a horizontal distance x and vertical distance y from its initial position at $t = t_i$. Light strikes this point at an angle θ_1 (from the horizontal axis) and reflects at an angle θ_2. All points on the surface are assumed to undergo the same displacement; if this is not the case, the following results must be averaged over all displacements that contribute to the measurement.

For each location of the object point, the optical transit time equals the difference between the initial transit time (subscript "i") and the change in the optical path length.

$$T_1 + T_2 = T_{1i} + T_{2i} - \frac{L_1 + L_2}{c_0} \tag{4.4}$$

Assuming that the object moves slowly compared to the speed of light, the apparent transit time may be approximated from Equation 3.3.

$$T^* \approx \frac{x_r^* - x^*}{c_0} = T_i^* - \frac{x^*}{c_0} \tag{4.5}$$

Using Equation 4.3 and the fact that $2T_i^* = T_{1i} + T_{2i}$ leads to the following expression.

$$x^* = \frac{L_1 + L_2}{2} \tag{4.6}$$

From the geometry shown in Figure 4.1:

$$\begin{aligned} L_1 + L_2 &= H\left(\sin(\eta - \theta_1) + \sin(\eta + \theta_2)\right) \\ &= H\left(\sin\eta\cos\theta_1 - \cos\eta\sin\theta_1 + \sin\eta\cos\theta_2 + \cos\eta\sin\theta_2\right) \\ &= x\left(\cos\theta_2 + \cos\theta_1\right) + y\left(\sin\theta_2 - \sin\theta_1\right) \end{aligned}$$

so the apparent position of the mirror may be expressed as:

$$x^* = \frac{x}{2}\left(\cos\theta_2 + \cos\theta_1\right) + \frac{y}{2}\left(\sin\theta_2 - \sin\theta_1\right) \tag{4.7}$$

which yields the following apparent velocity.

$$v^* = \frac{v_x}{2}\left(\cos\theta_2 + \cos\theta_1\right) + \frac{v_y}{2}\left(\sin\theta_2 - \sin\theta_1\right) \tag{4.8}$$

48

$$\sin \eta = \frac{x}{H} \qquad\qquad \cos(\pi/2 - \eta + \theta_1) = \frac{L_1}{H}$$

$$\cos \eta = \frac{y}{H} \qquad\qquad \cos(\pi/2 - \eta - \theta_2) = \frac{L_2}{H}$$
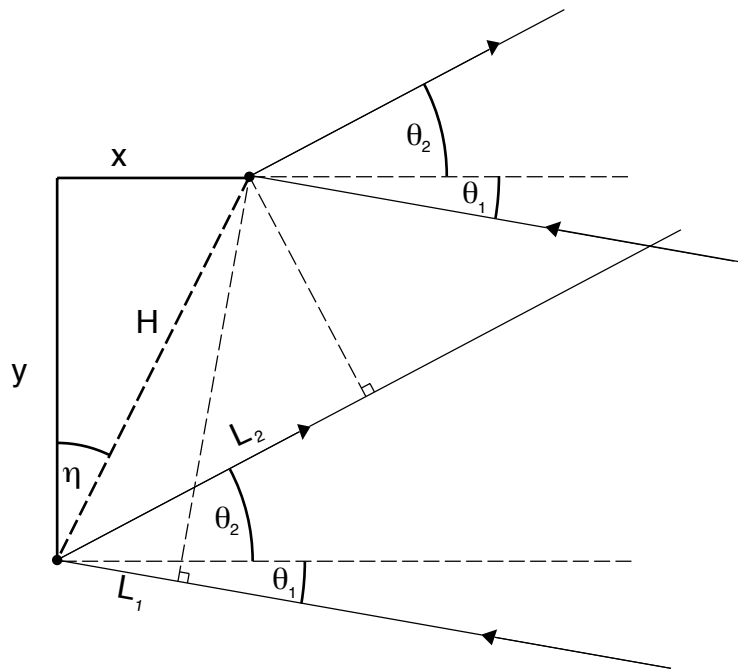
Figure 4.1. Non-normal illumination and reflection geometry.

4.1.2 Diffuse reflectors

Suppose that a diffuse surface is illuminated normally ($\theta_1 = 0$) and the reflected light is collected over range of angles, as in many fiber coupled measurements [31]. For light reflected at angle θ_2, the apparent velocity is given by:

$$v^* = v_x \frac{1 + \cos \theta_2}{2} \tag{4.9}$$

where it is assumed (for now) that the mirror has a transverse velocity of zero. If $\theta_2 \leq \theta_m$ and θ_m is sufficiently small, one can estimate the apparent velocity by substituting the average angle ($\theta_m/2$) in the above expression. For $\theta_m < 7°$, the apparent velocity correction is less than 0.1% [31].

For larger angle measurements, the apparent velocity must be averaged over the reflected radiance L. For a perfectly diffuse (*i.e.* Lambertian [14]) surface, L is a constant at all angles, so apparent velocity is simply averaged over the solid angle.

$$\langle v^* \rangle = \frac{\int v^* \, L \, d\Omega}{\int L \, d\Omega} \tag{4.10}$$

For azimuthal symmetry, this can be reduced to a simple form.

$$\langle v^* \rangle = \frac{v_x}{2} \frac{\int_0^{\theta_m} (1 + \cos \theta_2) \sin \theta_2 \, d\theta_2}{\int_0^{\theta_m} \sin \theta_2 \, d\theta_2} = \frac{v_x}{2} \left(1 + \frac{1 + \cos \theta_m}{2} \right) \tag{4.11}$$

This correction is important when a fast lens is used to increase the amount of light reaching the VISAR [32]. For example, a $F/1$ collection lens ($\theta_m \approx 26.6°$) leads to a velocity correction of 2.6%.

In general, the apparent velocity is a function of both longitudinal and transverse motion of a surface. For normal illumination and reflection, velocity measurement is insensitive to the transverse motion:

$$v_1^* = v_x \tag{4.12}$$

whereas reflection at an angle involves both velocity components.

$$v_2^* = \frac{v_x}{2} (\cos \theta_2 + 1) + \frac{v_y}{2} (\sin \theta_2) \tag{4.13}$$

This analysis has been applied to diffuse reflectors [33] as well surfaces deposited with a diffraction grating [34]; in the latter case, light collection is restricted to specific angles determined by the grating density, but otherwise the analysis is similar.

4.1.3 Specular reflectors

The apparent velocity relationship for a specular surface $(\theta_1 = \theta_2)$ is quite simple.

$$v^* = v_x \cos \theta_1 \tag{4.14}$$

When a specular surface is illuminated over a range of angles, integration is performed on either the illumination or the collection angle, whichever is more restrictive. For uniform illumination over a maximum angle θ_m and azimuthal symmetry, the apparent velocity may be written as follows.

$$\langle v^* \rangle = v_x \frac{\int_0^{\theta_m} \cos\theta \sin\theta \, d\theta}{\int_0^{\theta_m} \sin\theta \, d\theta} = \frac{v_x}{2}(1 + \cos\theta_m) \tag{4.15}$$

In this case, the correction is less than 0.1% for $\theta_m < 3.5°$; this range is smaller than for a diffuse reflector because angular corrections occur during both illumination and collection. Note that specular measurements are insensitive to transverse motion at all illumination angles.

4.2 Window corrections

An important class of velocity corrections occur for measurements that involve optical windows. Light passing through the window travels more slowly than it would in vacuum, altering the optical transit time and leading to substantial velocity corrections. Window corrections are typically much larger than angular corrections, so the latter will be omitted from the discussion.

4.2.1 General problem

Suppose that the light path in a velocity measurement contains a dielectric window as shown in Figure 4.2. For normal incidence and reflection, the actual and apparent transit times may be written as follows.

$$T^* = \int_{x^*(t)}^{x_r^*} \frac{dx'}{c_0} = \frac{x_r - x^*(t)}{c_0} \tag{4.16}$$

$$T_1 + T_2 = -\int_{x_r}^{x(t)} \frac{dx'}{c_1(x',t)} + \int_{x(t)}^{x_r} \frac{dx'}{c_2(x',t)} \approx 2\int_{x(t)}^{x_r} \frac{dx'}{c(x',t)} \tag{4.17}$$

Here c_i $(i = 1, 2)$ is the local speed of light during the i−th transit; if all motion in the measurement is much slower than the speed of light, these functions are essentially the same. Substitution of these expressions into Equation 4.3 yields the apparent position in terms of the real position and local refractive index $n = c_0/c$:

$$x_r^* - x^*(t) = \int_{x(t)}^{x_r} n(x',t)dx' \tag{4.18}$$
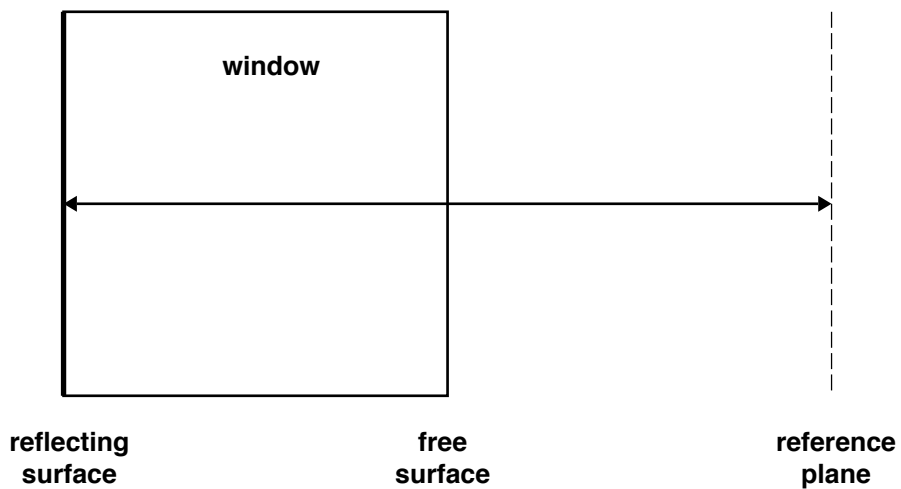
Figure 4.2. Velocity measurement through a window.

Table 4.1. Common window corrections

Material	Correction (a)	Reference
z-axis quartz	1.083 (514.5 nm)	35
c-axis sapphire	1.76 (532 nm)	36
	1.786 (532 nm)	37
	1.783 (532 nm)	38
	1.785 (532 nm)	39
a-axis sapphire	1.844-1.896 (514.5 nm)	40
$\langle 100 \rangle$ lithium fluoride	1.281 (514.5 nm)	41
	1.280 (532 nm)	36

which may be differentiated to determine the apparent velocity.

$$v^*(t) = -\frac{d}{dt}\left[\int_{x(t)}^{x_r} n(x',t)dx'\right] \tag{4.19}$$

For the configuration in Figure 4.2, Equation 4.19 can be divided into two integrals, one from the mirror to the window free surface located at $x_s(t)$ and the other from $x_s(t)$ to the reference plane [38, 42, 43].

$$v^*(t) = -\frac{d}{dt}\left[\int_{x(t)}^{x_s(t)} n(x',t)dx' + (x_r - x_s(t))\right]$$

$$= -\frac{d}{dt}\left[\int_{x(t)}^{x_s(t)} n(x',t)dx'\right] + v_s(t) \tag{4.20}$$

Here v_s is the window free surface velocity. Reduction of the remaining integral requires some knowledge of the refractive index profile in the window. Wave propagation simulations can be used to validate a particular refractive index model for a prescribed loading history, but in practice, window corrections are obtained analytically from one of the special cases described below.

4.2.2 Shocked windows

Equation 4.20 can be greatly simplified when the window is compressed by a single shock wave. Shock waves are nearly discontinuous compressions [1] that travel at a fixed velocity D in the lab frame. Behind the shock front, material is compressed to a constant state that travels at the mirror velocity; ahead of the front, the material is at rest. Under these conditions, Equation 4.20 can be written as follows:

$$v^* = -\frac{d}{dt}\left[n(x_D(t) - x(t)) + n_0(x_s - x_D(t))\right] \tag{4.21}$$

where n is the refractive index behind the shock front, $x_D(t)$ is the shock front position, n_0 is the refractive index ahead of the shock front, and x_s is the window free surface position (assumed to be constant). The resulting time derivative provides a simple relationship between the real mirror and shock velocities and the apparent mirror velocity [44].

$$v^* = n\ (v - D) + n_0\ D$$

$$= n\ v - (n - n_0)\ D \tag{4.22}$$

The arrival of the shock front at the window free surface changes the apparent velocity correction, and provides a distinct timing fiducial that can be used to calculate the shock velocity [35]. If the compressed refractive index is known, then the true mirror velocity can be determined.

$$v = \frac{v^* + (n - n_0)\ D}{n} \tag{4.23}$$

53

Alternatively, the compressed refractive index can be determined if the true mirror velocity is known.

$$n = \frac{v^* - n_0\,D}{v - D} \tag{4.24}$$

When combined with the jump conditions [1], this result may be used to determine refractive index as a function of density.

Under strong shock compression, an initially transparent material may become conductive and highly reflective (*e.g.*, deuterium [45]). This changes the apparent velocity calculation as light is reflected by the shock front rather than the original interface. Reexamination of Equation 4.20 shows that the correction is simply the refractive index ahead of the shock front.

$$D^* = -\frac{d}{dt}\left[n_0\,(x_s - x_D(t)) \right] = n_0\,D \tag{4.25}$$

4.2.3 Linear window materials

If the refractive index of the material is a function of local density only:

$$n = a + b\rho \tag{4.26}$$

then the apparent velocity can be expressed as follows [38, 42, 43].

$$v^* = -\frac{d}{dt}\left[a(x_s(t) - x(t)) + b \int_{x(t)}^{x_S} \rho(x',t)\,dx' \right] + v_s(t) \tag{4.27}$$

The density integral is proportional to the total mass of the window, and by mass conservation has a time derivative of zero (regardless of the window's density profile).

$$v^*(t) = -a(v_s(t) - v(t)) + v_s(t) = a\,v(t) - (a-1)\,v_s(t) \tag{4.28}$$

The true mirror velocity is thus linearly related to the apparent velocity.

$$v(t) = \frac{v^*(t) + (a-1)\,v_s(t)}{a} \tag{4.29}$$

Several common window corrections are given in Table 4.1.

When the window free surface is stationary, velocity corrections can be incorporated into the fringe constant. For example, the "sapphire VPF" of VISAR is the actual fringe constant (the "free surface VPF") divided by the window correction for sapphire. Although this approach is convenient in many situations, caution is required if the free surface begins to move during the experiment. When light passes through more than one window, additional care must be taken to use the proper correction during each stage of the analysis.

CHAPTER 5

VISAR characterization and performance

Beyond the underlying interferometer theory presented in Chapter 2, interpretation of a VISAR measurement relies on interferometer characterization and performance assessment. Characterization describes measurements of the interferometer and its output signals needed in the analysis process, the most important examples being the delay time and ellipse parameters. Performance assessment reveals how well a VISAR operates during a measurement, and can be described by dynamic contrast and the limiting fringe shift precision.

5.1 VISAR delay time

The delay time of a VISAR is defined by the condition of equal virtual length (Section 2.2). Although the interferometer contains distinct physical path lengths L_1 and L_2 (corresponding to interferometer legs containing M1 and M2 in Figure 2.4), the virtual distance of the second leg is shortened by the etalon. For maximum accuracy, this relationship must be corrected slightly to account for dispersion effects and delays in other components of the VISAR.

5.1.1 Ideal case

The condition of equal virtual lengths may be expressed as:

$$L_1 = L_2 - h + \frac{h}{n} \tag{5.1}$$

where h is the physical length and n is the refractive index of the etalon. The total transit time of the first leg is simply the ratio of path length to the vacuum speed of light:

$$t_1 = 2L_1/c_0 \tag{5.2}$$

while the total transit time for the second leg involves the etalon's refractive index.

$$t_2 = 2\left(\frac{L_2 - h}{c_0} + \frac{nh}{c_0}\right) \tag{5.3}$$

Combining these transit times with Equation 5.1 yields the delay time, which is purely a function of the etalon's size and refractive index.

$$\tau \equiv t_2 - t_1 = \frac{2h}{c_0}\left(n - \frac{1}{n}\right) \tag{5.4}$$

VISAR etalons are typically of order 0.1 m in length, yielding delay times of less than 1 ns. With some effort, longer delay times are also possible [8].

5.1.2 Dispersion correction

Systematic errors of several percent are often found when the VISAR delay time is calculated from Equation 5.4 [46]. These errors stem etalon dispersion, a subtle effect overlooked in the preceding analysis. To account for dispersion, it is important to distinguish the unshifted laser light in a VISAR (which is used during initial setup) from the Doppler shifted light collected during a measurement.

For unshifted laser light, the condition of equal virtual path length (Equation 5.1) is given in terms of the refractive index n at the laser operating wavelength λ_0.

$$L_1 = L_2 - h + \frac{h}{n} \tag{5.5}$$

The first interferometer leg is assumed to be free of dispersion, so the traversal time is similar to the original derivation (Equation 5.2). The second interferometer path contains the etalon, so the transit time depends on the refractive index n', which may be different from n due to Doppler shifting.

$$t_2 = \frac{2}{c_0}\left(L_2 - h + n'h\right) \tag{5.6}$$

$$\tau = t_2 - t_1 = \frac{2h}{c_0}\left(n' - \frac{1}{n}\right) \tag{5.7}$$

Doppler shifted wavelengths (Equation 3.1) in a VISAR measurement are not substantially different from the laser operating wavelength, so it is reasonable to define n' by a linear expansion about λ_0.

$$n' \approx n + \left.\frac{dn}{d\lambda}\right|_{\lambda_0}(\lambda - \lambda_0) = n - \left(2\lambda_0\left.\frac{dn}{d\lambda}\right|_{\lambda_0}\right)\frac{v}{c_0} \tag{5.8}$$

The Doppler shifted interferometer delay can then be written as:

$$\tau = \frac{2h}{c_0}\left[n - \frac{1}{n} - 2\lambda_0\left.\frac{dn}{d\lambda}\right|_{\lambda_0}\frac{v}{c_0}\right] = \tau_0\left(1 + 2\delta\frac{v}{c_0}\right) \tag{5.9}$$

56

where τ_0 is the unshifted delay time and δ is a dimensionless parameter for a given etalon material and operating wavelength (*e.g.,* $\delta = 0.0339$ for fused silica at 514.5 nm [46]).

$$\delta = -\frac{n}{n^2 - 1} \lambda_0 \left.\frac{dn}{d\lambda}\right|_{\lambda_0} \tag{5.10}$$

Note that in a dispersive VISAR, there is no single delay time; instead, the interferometer delay depends on the velocity at an earlier time. This subtlety drops out of the VISAR approximation (Section 3.3), leading to a simple correction of $1 + \delta$ in the fringe constant. Inverse VISAR analysis (Section 3.2) does not lead to such simplification, and dispersion effects are much harder to deal with than in the VISAR approximation.

5.1.3 Precision considerations

Fringe constant precision is dictated by the characterization of the VISAR delay time. In principle, the delay could be measured directly by timing the passage of a laser pulse through the interferometer. However, such a measurement would require extremely fast pulses and detector systems to achieve the precision attainable with physical measurements of the etalon. For a well characterized etalon, the fringe constant can be determined to within 0.1% [31].

For maximum precision, the delay time calculation must include all unbalanced elements of the VISAR system. The 1/8 wave plate and primary beamsplitter are key examples of unbalanced elements. The total delay time is given by the summation of the individual delay times of each element, which are assumed to all be contained in the second leg of the interferometer.

$$\tau = \tau_e \left(1 + 2\delta_e \frac{v}{c_0}\right) + \tau_{wp} \left(1 + 2\delta_{wp} \frac{v}{c_0}\right) + \tau_{bs} \left(1 + 2\delta_{bs} \frac{v}{c_0}\right) + \tau_m \tag{5.11}$$

The unshifted delay times for the etalon (τ_e) and wave plate (τ_{wp}) are given by Equation 5.4; for the beam splitter, the unshifted delay time is half of Equation 5.4. The final term, $\delta_m = 2\Delta L/c_0$, represents the time delay arising from mirror misplacement. Contributions from each element can be collected into a total unshifted delay τ_0 and effective dispersion δ to match Equation 5.9.

$$\tau_0 = \tau_e + \tau_{wp} + \tau_{bs} + \tau_m \tag{5.12}$$

$$\delta = \frac{\delta_e \tau_e + \delta_{wp} \tau_{wp} + \delta_{bs} \tau_{bs}}{\tau_e + \tau_{wp} + \tau_{bs} + \tau_m} \approx \delta_e \tag{5.13}$$

Since the etalon tends to be substantially larger than the other elements, the effective dispersion is approximately equal to the etalon dispersion.

As an example, consider the error created by a mirror misplacement ΔL in a VISAR system

with an intended fringe constant K_0.

$$K_0 = \frac{\lambda_0}{2(1+\delta)\tau_e} \qquad K = \frac{\lambda_0}{2(1+\delta)(\tau_e + \tau_m)}$$

$$\frac{K}{K_0} = \frac{1}{1 + \tau_m/\tau_e} \approx 1 - 4(1+\delta)\frac{K_0}{c_0}\frac{\Delta L}{\lambda_0} \tag{5.14}$$

The correction scales with K/c_0, so large fringe constants require precise mirror precision to maintain reasonable uncertainty. For a 1 km/s fringe constant, the interferometer must be constructed to better than 75 wavelengths (about 0.04 mm for $\lambda_0 = 532$ nm) to attain 0.1% precision.

5.2 Ellipse parameters

The basic function of a VISAR system is to determine the phase difference $\Phi(t)$ from the quadrature signals D_x and D_y.

$$\tan\Phi(t) = \tan\varepsilon + \frac{D_y(t) - y_0\,A_x}{D_x(t) - x_0\,A_y}\sec\varepsilon \tag{5.15}$$

Obviously, this calculation requires knowledge of ellipse parameters—x_0, y_0, A_x, A_y, and ε—for a particular interferometer configuration. Ideally, the VISAR ellipse should be made to be a perfect circle, but this is not always possible for a variety of reasons (*e.g.*, a shared wave plate in a multi-channel VISAR cannot optimize ε simultaneously on all channels).

In principle, each ellipse parameter could be determined by combining the power losses and/or phase shifts for each optical component in a VISAR. Better results are obtained through characterization measurements that directly probe the coupling parameters. Two types of ellipse characterization will be discussed here: ellipse fitting and parameter constraints. The first method is a general approach used to simultaneously determine all five ellipse parameters. The second method constrains specific ellipse parameters to some desired value (*e.g.*, $x_0 = 0$). At the end of this section, the two methods will be combined to show how the ellipse parameters can be obtained with maximum precision.

5.2.1 Ellipse fitting

Ellipses are a type of conic section, *i.e.* curves described by:

$$F(x,y) = ax^2 + bxy + cy^2 + dx + ey + f = 0 \tag{5.16}$$

where the value of $b^2 - 4ac$ must be negative [28]. The six conic section parameters can be expressed in terms of the five VISAR ellipse parameters as follows.

$$a = A_y^2 \tag{5.17}$$

$$b = 2A_xA_y\sin\varepsilon \tag{5.18}$$

$$c = A_x^2 \tag{5.19}$$

$$d = -2A_y^2x_0 - 2A_xA_yy_0\sin\varepsilon \tag{5.20}$$

$$e = -2A_x^2y_0 - 2A_xA_yx_0\sin\varepsilon \tag{5.21}$$

$$f = A_y^2x_0^2 + 2A_xA_yx_0y_0\sin\varepsilon + A_x^2y_0^2 - A_x^2A_y^2\cos^2\varepsilon \tag{5.22}$$

The reverse calculation is possible but requires some caution. Since Equation 5.16 may be multiplied by an arbitrary factor, it is important that parameter ratios be used in the conversion process.

$$\varepsilon = \arcsin\frac{b}{\sqrt{4ac}} \tag{5.23}$$

$$x_0 = \frac{eb - 2cd}{4ac - b^2} \tag{5.24}$$

$$y_0 = \frac{bd - 2ae}{4ac - b^2} \tag{5.25}$$

$$A_x = \sec\varepsilon\sqrt{x_0^2 + \frac{b}{a}x_0y_0 + \frac{c}{a}y_0^2 - \frac{f}{a}} \tag{5.26}$$

$$A_y = \sec\varepsilon\sqrt{\frac{a}{c}x_0^2 + \frac{b}{c}x_0y_0 + y_0^2 - \frac{f}{c}} \tag{5.27}$$

The goal of an ellipse fit is to identify parameters that best represent a set of (x, y) data. A common approach for determining the best fit is to minimize χ, the root mean square of Equation 5.16 over N data points.[1]

$$\chi^2 = \frac{1}{N^2}\sum_{i=1}^{N}F^2(x_i, y_i) \tag{5.28}$$

Ellipse fits are often performed on the quadrature signals obtained in a particular VISAR measurement. Ellipse data may also be obtained prior to a measurement by illuminating a VISAR with purely coherent light (of fixed amplitude) while moving one mirror of the interferometer over half an optical wavelength or more. In either case, ellipse fitting may be performed as a direct or an iterative process.

Direct ellipse fitting

Direct ellipse fitting utilizes the fact that $F(x, y)$ is linear with respect to the six conic section parameters (Equation 5.16). Hence, the parameter values that minimize χ^2 may

---

[1]Alternate definitions of χ, which rely on residual functions other than $F(x_i, y_i)$ or use the median of $F(x_i, y_i)$, may also be used [47]. Although more computationally expensive, such alternatives can reduce certain biases in the fitting process. More comprehensive discussion of this topic may be found in Ref. 48.

be found by linear least squares methods, which reduce the optimization problem to matrix manipulation [49]. In its most basic form, this approach does not guarantee that the result is an ellipse as the value of $b^2 - 4ac$ can be positive. Ellipse specific fitting was first achieved by Fitzgibbon *et al.* [50], who found that adding the constraint $b^2 - 4ac < 0$ transforms the optimization into an eigenvalue problem. A numerically robust version of Fitzgibbon's algorithm proposed by Halíř and Flusser [51] is used in the following examples.

A number of fits are shown in Figure 5.1 to demonstrate the utility of direct ellipse fitting,. The left column contains three noise free ellipses with different parameter choices: a perfect circle (A), a skewed ellipse with $\varepsilon = \pi/16$ (D), and a skewed ellipse with an aspect ratio of $4/3$ and $\varepsilon = \pi/8$ (G). The center (B, E, and H) and right (C, F, and I) columns contain similar ellipses with different noise levels (5% and 10%, respectively). The direct fit captures the general shape of each data set, and in the noise free cases, reproduces the original ellipse parameters within numerical precision. When noise is added, the fit parameters vary from the original values by several percent; typically, the variations are less than or comparable to the noise level. Rigorous characterization requires broader study over a wide array of parameter sets, noise levels, and noise classes, but these results suggest that the direct fitting method is sound.

One consideration in using the direct fitting method is how it deals with partial ellipse data, a common situation in VISAR measurements. Figure 5.2 shows the ellipses from the preceding discussion (noise levels set to 5%) with some data omitted. When the data spans half of the ellipse (A, D, and G), the direct fitting routine captures the general shape but does not precisely reproduce the correct ellipse. When only a quarter of the ellipse is present (B, E, and H), the direct fit is substantially different from the original ellipse. The fraction of an ellipse needed for reasonable behavior depends on the noise level [51], but there is a systematic problem with the direct fitting method when data is clustered along one portion of the ellipse. Data clusters on opposite sides of the ellipse (C, F, and I) lead to more reasonable results, although there is a reduction of parameter accuracy.

Iterative ellipse fitting

Iterative ellipse fitting is a repetitive process used to optimize the ellipse parameters. Each iteration involves the following tasks.

1. Choose a set of ellipse parameters (x_0, y_0, A_x, A_y, and ε).

2. Calculate the corresponding conic section parameters (a, b, c, d, e, and f).

3. Evaluate the function $F(x, y)$ (Equation 5.16) at each data point.

4. Evaluate the residual error χ^2.

5. Choose a new set of ellipse parameters that will hopefully make χ^2 smaller and repeat steps $2 - 4$ until some convergence criterion is met.
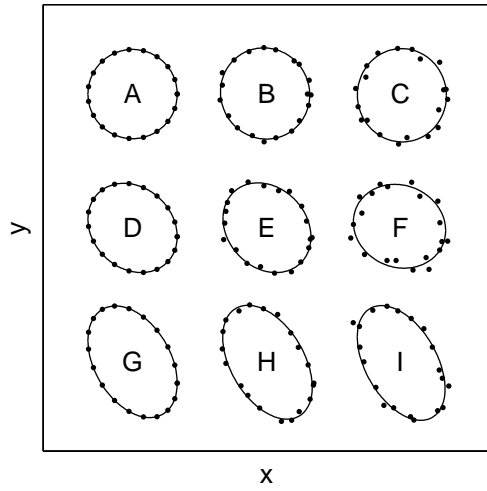
Figure 5.1. Direct ellipse fitting with noisy signals.
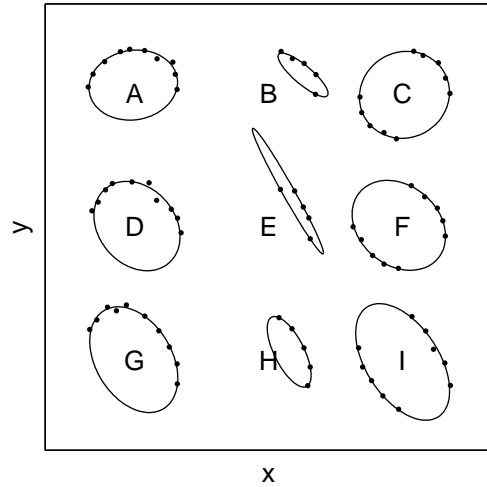
Figure 5.2. Direct ellipse fitting with missing data.
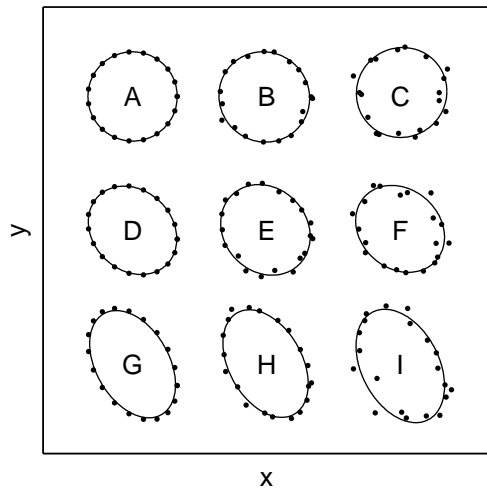
Figure 5.3. Iterative ellipse fitting with noisy signals.
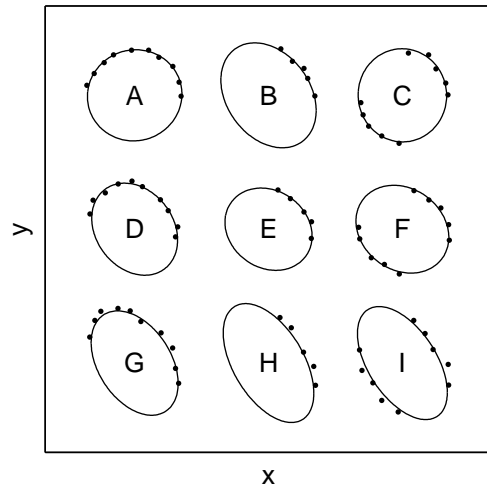
Figure 5.4. Iterative ellipse fitting with missing data

Unlike direct ellipse fitting, iterative ellipse fitting may never reach a final conclusion. The process could iterate around a local minimum of χ^2 forever without reaching the best fit curve of interest. The probability of reaching the true minimum (and the number of iterations required to get to that minimum) is related to the starting conditions. The difficulties of the iterative method can be mitigated through the use of different optimization schemes, the details of which are beyond the scope of this work; the interested reader is directed to Ref. 49. Despite the practical challenges of iterative optimization, it is straightforward to fix specific ellipse parameters in the process and implement different residual functions, features that are difficult (perhaps impossible) to achieve with the direct ellipse fit.

For complete or nearly complete ellipse data, the direct and iterative methods yield quite similar results. Figure 5.3 shows iterative ellipse fits to noise-free data using a direct ellipse as the initial guess; the resulting parameters from these two approaches differ by a negligible amount. As noise is added, the two methods diverge slightly, though the discrepancy tends to be much smaller than the noise level. The actual difference between the two methods depends the specific optimization routine and the nature/magnitude of the signal noise and is beyond this scope of this work.

To illustrate situations when iterative fitting is superior to the direct method, consider the partial ellipse fits shown in Figure 5.4. The ellipses in this figure are identical to the previous discussion for Figure 5.4 using an iterative ellipse fit rather than the direct method. In the iterative fits, the ellipse center was fixed at the precise value for each data set. Although the plots in Figure 5.2 do not represent an exhaustive comparison between the two fitting methods, they suggest that iterative fitting is better suited to partial ellipse data because of the ability to constrain specific ellipse parameters. Note that in spite of this advantage, iterative fitting requires more work on the part of the user to provide a good initial guess. In many cases, it would be advisable to perform a direct fit initially, then use that result as the guess for an iterative method. When this is not possible, one should generate a guess by visual inspection, *i.e.* plot ellipses with different parameter sets to find a reasonable match with the data. This process may require some trial and error as certain guesses converge to a proper result easily, while slightly different guesses perform very badly. The human eye and good judgment are often needed to determine which ellipse comprises the best fit curve.

5.2.2 Parameter constraints

Parameter constraints represent a means of forcing an ellipse parameter to some desired value, rather than determining that parameter from a best fit ellipse. A push-pull VISAR system (Section 2.4) is the primary example when ellipse parameters must be enforced. Specifically, the center of the ellipse must be fixed at the origin, regardless of the input intensity. By inspection of Equations 2.46–2.47, this condition is met by the following

scaling factor ratios.

$$\frac{\eta_{1B}}{\eta_{1A}} = \frac{\hat{a}_{11}^2 + \hat{a}_{21}^2}{\hat{b}_{11}^2 + \hat{b}_{21}^2} \tag{5.29}$$

$$\frac{\eta_{2B}}{\eta_{2A}} = \frac{\hat{a}_{12}^2 + \hat{a}_{22}^2}{\hat{b}_{12}^2 + \hat{b}_{22}^2} \tag{5.30}$$

Furthermore, the aspect ratio (A_x/A_y) can be set to unity by the following choice of scaling factors.

$$\frac{\eta_{2A}}{\eta_{1A}} = \frac{\hat{a}_{11}\hat{a}_{21} + \dfrac{\eta_{1B}}{\eta_{1A}}\hat{b}_{11}\hat{b}_{21}}{\hat{a}_{12}\hat{a}_{22} + \dfrac{\eta_{2B}}{\eta_{2A}}\hat{b}_{12}\hat{b}_{22}} \tag{5.31}$$

One approach for determining the coupling constants is expose a VISAR to incoherent light, which eliminates interference. Measurements made under such conditions (denoted here by a bar):

$$\bar{D}_{1A} = \left(\hat{a}_{11}^2 + \hat{a}_{21}^2\right)\bar{I}_0 \tag{5.32}$$

$$\bar{D}_{2A} = \left(\hat{a}_{12}^2 + \hat{a}_{22}^2\right)\bar{I}_0 \tag{5.33}$$

$$\bar{D}_{1B} = \left(\hat{b}_{11}^2 + \hat{b}_{21}^2\right)\bar{I}_0 \tag{5.34}$$

$$\bar{D}_{2B} = \left(\hat{b}_{12}^2 + \hat{b}_{22}^2\right)\bar{I}_0 \tag{5.35}$$

can be used to yield two scaling ratios.

$$\frac{\eta_{1B}}{\eta_{1A}} = \frac{\bar{D}_{1A}}{\bar{D}_{1B}} \tag{5.36}$$

$$\frac{\eta_{2B}}{\eta_{2A}} = \frac{\bar{D}_{2A}}{\bar{D}_{2B}} \tag{5.37}$$

Unfortunately, the third constraint (unity aspect ratio) cannot be applied exactly because each incoherent light measurement contains several coupling parameters.

An alternate method for determining the coupling constants is to operate a VISAR with completely coherent input while blocking one leg of the interferometer [20]; obviously, this method requires consistent input intensity when the alternate leg is blocked. This process yields eight signals, each of which is proportional to the square of a single coupling constant, as shown in the following example.

$$\bar{D}_{1A}^{(1)} = \hat{a}_{21}^2 \bar{I}_0 \tag{5.38}$$

The superscript "(1)" indicates that the measurement is performed with the first path blocked; the corresponding measurement for the same detector with the other leg blocked would be

$\bar{D}_{1A}^{(2)}$. These eight measurements provide sufficient information for all three constraints.

$$\frac{\eta_{1B}}{\eta_{1A}} = \frac{\bar{D}_{1A}^{(1)} + \bar{D}_{1A}^{(2)}}{\bar{D}_{1B}^{(1)} + \bar{D}_{1B}^{(2)}} \tag{5.39}$$

$$\frac{\eta_{2B}}{\eta_{2A}} = \frac{\bar{D}_{2A}^{(1)} + \bar{D}_{2A}^{(2)}}{\bar{D}_{2B}^{(1)} + \bar{D}_{2B}^{(2)}} \tag{5.40}$$

$$\frac{\eta_{2A}}{\eta_{1A}} = \frac{\sqrt{\bar{D}_{1A}^{(1)}\bar{D}_{1A}^{(2)}} + \frac{\eta_{1B}}{\eta_{1A}}\sqrt{\bar{D}_{1B}^{(1)}\bar{D}_{1B}^{(2)}}}{\sqrt{\bar{D}_{2A}^{(1)}\bar{D}_{2A}^{(2)}} + \frac{\eta_{2B}}{\eta_{2A}}\sqrt{\bar{D}_{1B}^{(1)}\bar{D}_{1B}^{(2)}}} \tag{5.41}$$

There are alternative ways of enforcing the correct scaling in a push-pull VISAR in certain types of measurements. For example, if a portion of a VISAR measurement contains a continuously varying phase difference, with no incoherent light and minimal variations variations in coherent intensity, it may be possible to visually scale the detector signals so that all oscillations are consistent. However, the beam blocking method is recommended for greatest accuracy.

5.2.3 Combined characterization

Ellipse fitting can determine all the ellipse parameters, but there is a resolution compromise because the fit has five degrees of freedom. At the same time, parameter constraints are precise but only apply to certain quantities—x_0, y_0, and A_y/A_x—and thus cannot completely characterize the ellipse. Hence, one must always perform some type of ellipse fit, but the use of parameter constraints can significantly improve the resolution of the remaining quantities.

A push-pull VISAR characterized with beam blocking is an important special case where ellipse constraints reduce the degrees of freedom considerably. In such a system, the quadrature signals are perfectly centered about the origin and have an aspect ratio of unity. Under these conditions, the mathematical description of the ellipse (Equation 5.16) becomes quite simple:

$$x^2 + 2\sin\varepsilon\, xy + y^2 - A^2\cos\varepsilon = 0 \tag{5.42}$$

where $A = A_x = A_y$. With some minor manipulation, this can be expressed as a linear fit.

$$\underbrace{x^2 + y^2}_{Y} = -2\sin\varepsilon\, \underbrace{xy}_{X} + A^2\cos^2\varepsilon \tag{5.43}$$

The slope of Y versus X yields the value of ε, while the intercept can be used to determine A. Hence, it possible to use a set of quadrature signals to directly determine the size and quadrature error. The uncertainty in these parameters can also be determined quantitatively [52].

5.3 Dynamic contrast

Contrast was introduced in Chapter 2 to characterize the degree of interference in a VISAR system. The system contrast C_0 of a VISAR is related to its construction, and may be calculated from the signal outputs extremes.

$$C_0 = \frac{D_{max} - D_{min}}{D_{max} + D_{min}} \tag{5.44}$$

However, contrast may change during a VISAR measurement, such as when rapid changes exceed the detector bandwidth [20]. To quantify such behavior, the concept of contrast must be broadened to provide a time dependent characterization of the interferometer. A new quantity, the dynamic contrast, is defined to fulfill that role. Examples of dynamic contrast loss will then be described to indicate when this quantity is used to identify problems in a VISAR measurement.

5.3.1 Definitions

The difficulty with the basic definition of contrast (Equation 2.27) is the fact that one does not generally know the minimum and maximum detector signals at each moment in time. To get around this problem, recall that contrast in a WAMI (Section 2.2) is related to the ratio of oscillation amplitude to the offset. For a conventional VISAR, this suggests the following definition of dynamic contrast (assumed to be the same for both optical polarizations [19]).

$$D_x(t) = x_0 \left(1 + C(t)\cos\Phi(t)\right) \tag{5.45}$$
$$D_y(t) = y_0 \left(1 + C(t)\sin(\Phi(t) - \varepsilon)\right) \tag{5.46}$$

Elimination of Φ yields an expression for dynamic contrast in terms of the quadrature signals and the VISAR ellipse parameters.

$$\frac{C^2(t)}{\sec^2\varepsilon} = \left(\frac{D_x(t) - x_0}{x_0}\right)^2 + 2\left(\frac{D_x(t) - x_0}{x_0}\right)\left(\frac{D_y(t) - y_0}{y_0}\right)\sin\varepsilon + \left(\frac{D_y(t) - y_0}{y_0}\right)^2 \tag{5.47}$$

Note that the dynamic contrast is *similar* to the radius of the VISAR ellipse:

$$r^2 = (D_x(t) - x_0)^2 + (D_y(t) - y_0)^2 \tag{5.48}$$

but the two quantities are not proportional unless $\varepsilon = 0$ and $x_0 = y_0$. Although not immediately obvious from Equation 5.47, dynamic contrast is equivalent to the product of the system contrast and the coherent-total input intensity ratio (Section 2.3).

$$C(t) = C_0 \frac{I_c(t)}{I_0(t)} \tag{5.49}$$

Dynamic contrast must be modified somewhat for use in a push-pull VISAR as Equation 5.47 involves division by x_0 and y_0, both of which should be zero. A similar quantity $C'(t)$,

or pseudo-contrast, is used instead.

$$(C'(t))^2 = \sec^2 \varepsilon \left[D_x^2(t) + 2D_x(t)D_y(t)\sin\varepsilon + D_y^2(t) \right] \qquad (5.50)$$

Pseudo-contrast is proportional to the coherent intensity, not the total input intensity. For convenience, $C'(t)$ can be normalized by an arbitrary reference value.

5.3.2 Dynamic contrast loss

Since contrast is a measure of the coherent light available to an interferometer, any effect that decreases coherence will correspond to a reduction of dynamic contrast. Contrast may be lost through coherent signal decrease (*e.g.,* input power loss), incoherent signal increase (*e.g.,* blackbody emission), or multiphase interference [20]. The first two situations are relatively straightforward; the latter is more subtle and will be elaborated in the next subsection.

Contrast loss is commonly associated with rapid changes in a VISAR measurement, and may occur for several reasons. At extremely short times scales, photodetectors may be unable to follow the optical signals, resulting in signal transients that are convolution of the phase difference changes and the detector response [53]. Contrast loss may also occur due to transient unbalancing of light in each leg of the VISAR, where changes of the input power occur on time scales comparable to the interferometer delay. The latter example of contrast loss results from a shortcoming in standard VISAR analysis, not the measurement itself; refined analysis (Section 2.4.2) should eliminate this problem.

5.3.3 Multiphase interference

By its very construction, a VISAR system is ill-equipped to handle multiple coherent light sources. Measurements of a velocity distribution [54], over a broad angular range [32], or containing multiple light reflections (*e.g.,* a diffuse target mirror behind a shocked window [55]) may contain multiple coherent sources that reduce interferometer contrast. Narrow angle illumination and careful collection systems can be used to isolate specific coherent sources and maximize contrast. However, multiple coherent source measurements are not an optimal application of the VISAR, and are better suited for other diagnostics [10, 11].

To illustrate why multiple coherent sources yield low VISAR contrast, one must return to the basic operation of a Michelson interferometer. The output of the Michelson interferometer is given by Equation 2.9.

$$I(t) = \underbrace{a_1^2\, I_0(t-t_1) + a_2^2\, I_0(t-t_2)}_{\text{ellipse center}} + \underbrace{2a_1 a_2 \eta \left\langle E_c(t-t_1)E_c(t-t_2) \right\rangle}_{\text{ellipse size}} \qquad (5.51)$$

The first two terms contribute to the offset of a VISAR signal (the ellipse center), while the third contributes to the signals oscillation amplitude (ellipse size).

Suppose that E_c is a discrete sum of multiple coherent contributions[2].

$$E_c(t) = \sum_n A_n(t) \cos \phi_n(t) \tag{5.52}$$

The time average coherent electric field now becomes:

$$\langle E_c(t - t_1) E_c(t - t_2) \rangle = \left\langle \sum_n A_n(t - t_1) \cos \phi_n(t - t_1) \sum_m A_m(t - t_2) \cos \phi_m(t - t_2) \right\rangle$$

$$= \sum_n A_n(t - t_1) A_n(t - t_2) \langle \cos \phi_n(t - t_1) \cos \phi_n(t - t_2) \rangle$$

$$+ 2 \sum_{n \neq m} A_n(t - t_1) A_m(t - t_2) \langle \cos \phi_n(t - t_1) \cos \phi_m(t - t_2) \rangle \tag{5.53}$$

where the first summation contains the product of each coherent source with a time shifted version of itself and the second summation contains cross terms between different coherent contributions. Although each function $\phi_n(t)$ is itself coherent, these functions originate from different sources and are mutually incoherent [12]. Following the same logic leading to Equation 2.12 and assuming that A_n changes slowly over τ leads to the following result.

$$\langle E_c(t - t_1) E_c(t - t_2) \rangle = \sum_n \frac{A_n(t - t_1) A_n(t - t_2)}{2} \cos \Phi_n(t) \approx \sum_n \frac{A_n^2(t)}{2} \cos \Phi_n(t) \tag{5.54}$$

The total coherent power can be expressed as the sum of the power carried by each coherent term:

$$I_c(t) = \sum_n I_{c_n} = \frac{\eta A_n^2(t)}{2} \tag{5.55}$$

which can be compared to the time averaged field product.

$$\eta \langle E_c(t - t_1) E_c(t - t_2) \rangle \approx \sum_n I_{c_n}(t) \cos \Phi_n(t) \leq I_c(t) \tag{5.56}$$

The final inequality expresses a very basic fact: $\cos \Phi$ lies between -1 and 1, resulting in a summation of coherent power contributions that is smaller than the total coherent power input.

Following the logic leading to Equation 5.47 yields a generalization for the dynamic contrast.

$$\frac{C^2(t)}{C_0^2 \sec^2 \varepsilon} = \left(\sum_n w_n \cos \Phi_n(t) \right)^2 + \left(\sum_n w_n \cos \Phi_n(t) \right) \left(\sum_n w_n \sin(\Phi_n(t) - \varepsilon) \right) \sin \varepsilon$$

$$+ \left(\sum_n w_n \sin(\Phi_n(t) - \varepsilon) \right)^2 \tag{5.57}$$

---

[2]If a continuous phase distribution is present, the sum would be expressed as an integral and A_n would become a weighting function $A(n)$.

Here w_n represent the relative weight of each coherent contribution

$$w_n(t) \equiv \frac{I_{c_n}(t)}{I_0(t)} \quad \left(\sum_n w_n(t) = 1 \right) \tag{5.58}$$

For simplicity, suppose that the VISAR is configured with perfect quadrature ($\varepsilon = 0$).

$$
\begin{aligned}
\frac{C^2(t)}{C_0^2} &= \left(\sum_n w_n(t) \cos \Phi_n(t) \right)^2 + \left(\sum_n w_n(t) \sin(\Phi_n(t)) \right)^2 \\
&= \sum_n w_n^2(t) + 2 \sum_{n \neq m} w_n(t) \, w_m(t) \left[\cos \Phi_n(t) \cos \Phi_m(t) + \sin \Phi_n(t) \Phi_m(t) \right] \\
&= \sum_n w_n^2(t) + 2 \sum_{n \neq m} w_n(t) \, w_m(t) \cos \left[\Phi_n(t) - \Phi_m(t) \right]
\end{aligned} \tag{5.59}
$$

Since weights are non-negative, the maximum value of contrast occurs when all cosine terms equal unity.

$$\frac{C^2(t)}{C_0^2} \leq \sum_n w_n^2(t) + 2 \sum_{n \neq m} w_n(t) \, w_m(t) = \sum_n w_n(t) \sum_m w_m(t)$$

$$\frac{C^2(t)}{C_0^2} \leq 1 \tag{5.60}$$

The upper bound may only be reached when all phase difference values are the same, *i.e.* there is only one coherent contribution to the VISAR signal. When multiple coherent contributions are present, the dynamic contrast is less than the instrument contrast.

5.4 Precision limits

Recall that fringe shift is the normalized difference of the current and initial phase difference functions (Equation 3.19):

$$F(t) = \frac{\Phi(t) - \Phi(t_i)}{2\pi} \tag{5.61}$$

and phase difference is calculated from the inverse tangent of the quadrature signals (Equation 2.37).

$$\tan \Phi = \tan \varepsilon + \frac{D_y - y_0 \, A_x}{D_x - x_0 \, A_y} \sec \varepsilon \tag{5.62}$$

Two factors limit the precision with which fringe shift may be determined. First, the periodic nature of the tangent function creates an ambiguity in fringe shift. Second, the quadrature signal quality and ellipse parameter characterization limit the accuracy with which fringe shift can be calculated. The importance of each factor is tied to the fringe constant K: fringe ambiguity dominates for small values of K while fringe uncertainty dominates for large values of K.

5.4.1 Fringe ambiguity

Since the addition of 2π to the phase difference yields the same quadrature signals, the fringe shift is only specified within some integer offset.

$$F(t) = F_p(t) + N(t) \qquad (5.63)$$

Here $F_p(t)$ is a number between zero and unity calculated directly from Equations 5.61–5.62 and $N(t)$ is an integer-valued function. Non-integer values of $N(t)$ can be used to create gradual transitions over a specified rise time. While such smoothing leads to visually appealing results, there is no definitive criteria for what rise time should be used.

The value of $N(t)$ can be often resolved by logical means if contrast is maintained throughout the measurement. For example, data that wraps completely around the ellipse requires the addition of a fringe when $F(t)$ decreases by a factor of more than 0.5; such an addition merely reflects the limited output range of the inverse tangent function. Difficulties arise, however, if contrast is lost during portion of the measurement. Contrast loss is an indication that fringe addition (or subtraction) may be necessary, but it does not reveal how many fringes need to be added.

When dealing with fringe ambiguity, it is generally assumed that the VISAR approximation (Section 3.3) applies to the measurement.

$$v(t) = v_i + K\left[F_p(t) + N(t)\right] \qquad (5.64)$$

This relation provides some insight on how to add or subtract fringes. For example, suppose that the maximum possible velocity in a measurement is known. If this velocity is smaller than the fringe constant, then one can be certain that no fringes can be added. By the same token, maximum velocity estimates larger than the fringe constant provide an indication of the number of fringes that could be added to the measurement (v_{max}/K). A clear way to minimize ambiguity is to use fringe constants that exceed the maximum expected velocity in a measurement, but this may not be possible with a given VISAR system. Even when possible, the use of large fringe constants is not always desirable for reasons described in the next subsection.

Another method for dealing with fringe uncertainty is to measure velocity with two VISAR systems, each having a different fringe constant. Since the two measurements must yield the same result, there is a constraint on the number of fringes that can be added to either record.

$$v(t) = v_i + K_1\left[F_{p_1}(t) + N_1(t)\right] = v_i + K_2\left[F_{p_2}(t) + N_2(t)\right]$$
$$N_2(t) = \frac{K_1}{K_2}\left[F_{p_1}(t) + N_1(t)\right] - F_{p_2}(t) \qquad (5.65)$$

The integer N_1 must chosen such that N_2 is also an integer, so the above expression is more limiting than it might first appear. For best results, the fringe constants should chosen such that K_1/K_2 is not close to being an integer. Fringe addition/subtraction using multiple

69

VISAR measurements is typically performed by iterative visual inspection: velocities are calculated for both records in the absence of fringes, and fringes then added to each record to obtain consistency.

5.4.2 Fringe uncertainty

Once fringe ambiguity has been resolved, the limiting factor in VISAR resolution is the precision of $F_p(t)$, which is essentially a question of angular resolution on the VISAR ellipse. Visual fringe estimates better than 0.06 ($\Delta\Phi = 2\pi/16$) are easily achievable, and the limiting uncertainty is generally quoted as 0.02 ($\Delta\Phi = 2\pi/50$) or better [5].

Fringe shift uncertainty is dictated by quadrature signal and ellipse parameter uncertainty. These uncertainties affect both the current and the initial phase difference, so the fringe shift uncertainty is approximated by quadrature combination of the two phase difference uncertainties [52].

$$(\delta F(t))^2 \approx \left(\frac{\delta\Phi(t)}{2\pi}\right)^2 + \left(\frac{\delta\Phi(t_i)}{2\pi}\right)^2 \leq 2\left(\frac{\delta\Phi(t)}{2\pi}\right)^2 \tag{5.66}$$

The inequality stems from the fact that $\delta\Phi(t_i) \leq \delta\Phi(t)$ because signal averaging can be performed on the initial state without sacrificing time resolution. The uncertainty in phase difference can be approximated by a second quadrature summation:

$$(\delta\Phi)^2 \approx \left(\frac{\partial\Phi}{\partial D_x}\delta D_x\right)^2 + \left(\frac{\partial\Phi}{\partial D_y}\delta D_y\right)^2 + \left(\frac{\partial\Phi}{\partial x_0}\delta x_0\right)^2 + \left(\frac{\partial\Phi}{\partial y_0}\delta y_0\right)^2$$
$$+ \left(\frac{\partial\Phi}{\partial A_x}\delta A_x\right)^2 + \left(\frac{\partial\Phi}{\partial A_y}\delta A_y\right)^2 + \left(\frac{\partial\Phi}{\partial\varepsilon}\delta\varepsilon\right)^2 \tag{5.67}$$

which leads to the following fringe shift uncertainty.

$$4\pi^2(\delta F(t))^2 \approx \left(\frac{\partial\Phi}{\partial D_x}\delta D_x\right)^2 + \left(\frac{\partial\Phi}{\partial D_y}\delta D_y\right)^2 + 2\left(\frac{\partial\Phi}{\partial x_0}\delta x_0\right)^2 + 2\left(\frac{\partial\Phi}{\partial y_0}\delta y_0\right)^2$$
$$+ 2\left(\frac{\partial\Phi}{\partial A_x}\delta A_x\right)^2 + 2\left(\frac{\partial\Phi}{\partial A_y}\delta A_y\right)^2 + 2\left(\frac{\partial\Phi}{\partial\varepsilon}\delta\varepsilon\right)^2 \tag{5.68}$$

The factors of two indicate that ellipse parameter uncertainty affects both the initial and the current phase difference, whereas signal uncertainty affects primarily the current phase difference.

70

With some manipulation, the partial derivatives of Φ can be expressed as follows.

$$\left| \frac{\partial \Phi}{\partial x} \right| = \left| \frac{\partial \Phi}{\partial x_0} \right| = \frac{|\sin \Phi - \cos \Phi \tan \varepsilon|}{A_x} \tag{5.69}$$

$$\left| \frac{\partial \Phi}{\partial y} \right| = \left| \frac{\partial \Phi}{\partial y_0} \right| = \frac{|\cos \Phi \sec \varepsilon|}{A_y} \tag{5.70}$$

$$\left| A_x \frac{\partial \Phi}{\partial A_x} \right| = \left| A_y \frac{\partial \Phi}{\partial A_y} \right| = \frac{|\sin 2\Phi - \cos 2\Phi \tan \varepsilon - \tan \varepsilon|}{2} \tag{5.71}$$

$$\frac{\partial \Phi}{\partial \varepsilon} = \frac{\sin 2\Phi \tan \varepsilon + \cos 2\Phi + 1}{2} \tag{5.72}$$

Each derivative is a function of Φ, so fringe uncertainty depends on where a particular measurement falls on the VISAR ellipse. For example, uncertainty in the vertical center (y_0) has no impact on the calculated angle at $\Phi = \pi/2$ but considerable effect at $\Phi = 0$. Note that each expression has the form:

$$Q(z) = a \sin z + b \cos z + c \tag{5.73}$$

which averages to zero over the domain $0 \leq \Phi < 2\pi$, but has a non-zero square average.

$$\langle Q^2(z) \rangle = \frac{1}{2\pi} \int_0^{2\pi} (a \sin z + b \cos z + c)^2 dz$$
$$= \frac{a^2 + b^2}{2} + c^2 \tag{5.74}$$

By replacing the partial derivatives in Equation 5.68 with the appropriate square average, the fringe uncertainty simplifies to an expression that depends only on signal/ellipse parameter uncertainties, ellipse size/aspect ratio, and the quadrature error.

$$4\pi^2 (\delta F(t))^2 \approx \left[\frac{1}{2} \left(\frac{\delta D_x}{A_x} \right)^2 + \frac{1}{2} \left(\frac{\delta D_y}{A_y} \right)^2 + \left(\frac{\delta x_0}{A_x} \right)^2 + \left(\frac{\delta y_0}{A_y} \right)^2 \right] \sec^2 \varepsilon$$
$$+ \left[\left(\frac{\delta A_x}{A_x} \right)^2 + \left(\frac{\delta A_y}{A_y} \right)^2 \right] \frac{3 \sec^2 \varepsilon - 2}{4} + (\delta \varepsilon)^2 \frac{\sec^2 \varepsilon + 2}{4} \tag{5.75}$$

To illustrate the relative importance of each uncertainty contribution, suppose that the uncertainty ratios (*e.g.*, $\delta D_x / A_x$) are the same for each optical polarization.

$$4\pi^2 (\delta F(t))^2 \approx \underbrace{\sec^2 \varepsilon}_{F_1(\varepsilon)} \left(\frac{\delta D_x}{A_x} \right)^2 + \underbrace{2 \sec^2 \varepsilon}_{F_2(\varepsilon)} \left(\frac{\delta x_0}{A_x} \right)^2 + \underbrace{\frac{3 \sec^2 \varepsilon - 2}{2}}_{F_3(\varepsilon)} \left(\frac{\delta A_x}{A_x} \right)^2$$
$$+ \underbrace{\frac{\sec^2 \varepsilon + 2}{2}}_{F_4(\varepsilon)} (\delta \varepsilon)^2 \tag{5.76}$$

71

The functions $F_1(\varepsilon)$, $F_2(\varepsilon)$, $F_3(\varepsilon)$, and $F_4(\varepsilon)$ determine the sensitivity of the fringe uncertainty to each uncertainty contribution and are shown in Figure 5.5. From the plots, it is evident that fringe uncertainty is most sensitive to the ellipse center (δx_0). For $\varepsilon < \pi/4$ (45°), quadrature error uncertainty ($\delta\varepsilon$) is next in importance, followed by signal uncertainty (δD_x) and ellipse size (δA_x); for large quadrature errors, ellipse size and quadrature error uncertainty swap in their importance. All sensitivity factors diverge at $\varepsilon = \pi/2$ (90°), when quadrature is completely lost and the ellipse collapses to a straight line.

The limiting resolution of a VISAR measurement can be calcuated by considering a system with perfect quadrature and a perfectly characterized ellipse. Most VISAR signals are acquired with eight bit digitizers, so the smallest possible value of $\delta D_x/A_x$ is $1/256$.

$$\delta F \geq \frac{1}{256 \cdot 2\pi} \approx 0.0006 \quad \text{(8-bit acquisition)} \tag{5.77}$$

In practice, only six or seven bits effect bits are obtained, so the limiting resolution is more like 0.001-0.002. Fringe precision is further degraded by ellipse parameter uncertainty, the magnitude of which depends on the care with which a VISAR system is constructed and characterized. For a visually optimized VISAR ellipse, fractional ellipse parameter uncertainties (e.g., $\delta x_0/A_x$) are of order 0.01 and $\delta\varepsilon$ is of order 0.0175 (1°), which leads to a limiting fringe uncertainty of order 0.004.

General estimates of the fringe shift resolution can be made by assuming that all fractional uncertainties in a VISAR measurement are the roughly the same ($\delta D_x/A_x = \delta x_0/A_x = \delta A_x/A_x$). In this case, the fringe shift uncertainty can be plotted for various quadrature error uncertainties as shown in Figure 5.6. Three values of $\delta\varepsilon$ (0, 2.5°, and 5°) are shown to provide an estimate of the quadrature error uncertainty encountered in a real measurement. From these curves, it is reasonable to quote the working fringe shift resolution as 0.01-0.02 as originally quoted by Barker and Hollenback [5]. Further refinement is possible, but only if the fractional uncertainties are less than 0.02 and the quadrature error is known to better than 2°.

5.4.3 Velocity precision

Assuming that fringe ambiguity has been dealt with and the initial velocity (v_i) is zero, velocity uncertainty can be expressed as:

$$(\delta v)^2 = (K\ \delta F)^2 + (F\ \delta K)^2$$
$$\left(\frac{\delta v}{v}\right)^2 = \left(\frac{K}{v}\delta F\right)^2 + \left(\frac{\delta K}{K}\right)^2 \tag{5.78}$$

where δF is of order 0.01 and $\delta K/K$ is of order 0.001 ($0.005 - 0.01$ if window corrections are included [31]). For $K \approx v$, velocity uncertainty is approximately equal to fringe uncertainty, whereas velocity uncertainty is magnified for $K > v$ because the quadrature signals traverse a smaller portion of the VISAR ellipse.
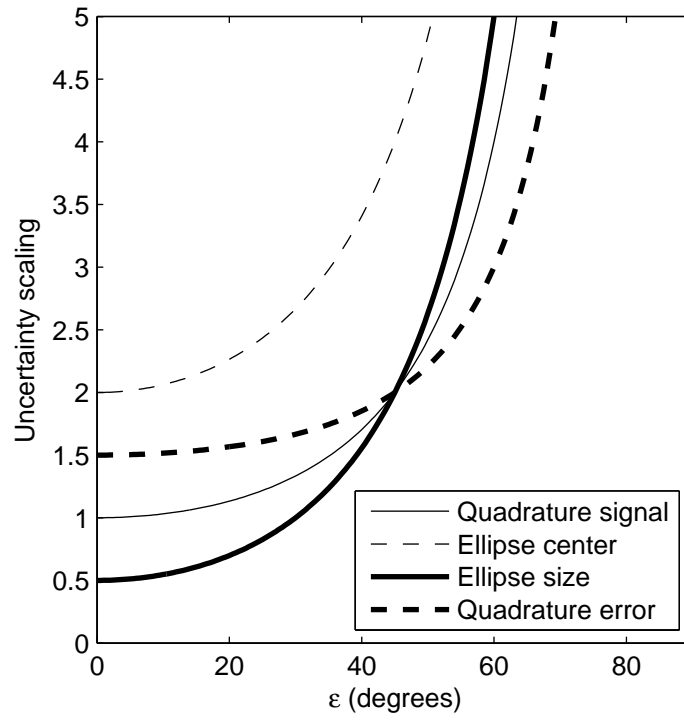
Figure 5.5. Ellipse parameter error sensitivity.
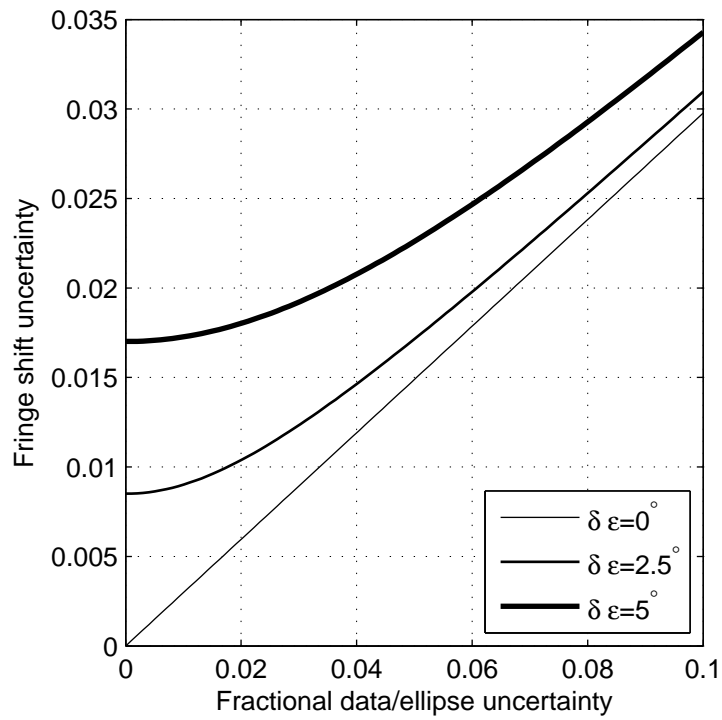
Figure 5.6. Fringe shift uncertainty.

From an uncertainty perspective, the ideal situation is for K to be much smaller than v, so that the quadrature data undergoes many rotations about the VISAR ellipse. There are limitations to doing this, however, as smaller values of K require larger interferometer delay times, which are difficult to attain in practical interferometer systems and can jeopardize the VISAR approximation (Section 3.3) in the extreme case. Moreover, minimizing the fringe constant to enhance velocity resolution is exactly the opposite action needed to reduce fringe ambiguity, so some compromise must be made.[3] In the dual fringe constant measurements described in the previous subsection, fringe ambiguities are resolved with the larger fringe constant system, while maximal velocity resolution is attained with the smaller fringe constant system.

---

[3]Another consideration in a single VPF measurement is that K be chosen such that the velocity history maps out the VISAR ellipse [38].

VISAR analysis is comprised of two basic operations—the calculation of fringe shift from measured quadrature signals and the calculation of mirror velocity. In addition to the theoretical basis for these operations, interpreting VISAR measurements also depends on practical issues, such as the characterization and performance of a VISAR system.

6.1 Fringe shift

The essential function of a Michelson interferometer is to superimpose light with a time delayed version of itself, so that the output intensity of the interferometer is related to the phase difference $\Phi(t)$.

$$\Phi(t) = \phi(t) - \phi(t - \tau) \tag{6.1}$$

Optical phase $\phi(t)$ describes the harmonic electric field variations of the input and is related to familiar quantities such as wavelength. Michelson interferometers are generally ill-suited for use velocity measurements because they yield spatially varying intensity (*i.e.* interference patterns) for imperfectly collimated input. Instead, the wide-angle Michelson interferometer (WAMI), which contains an uncompensated dielectric in one leg, is used to ensure uniform illumination of the output detectors.

Despite the basic utility of the WAMI, it can be difficult to separate optical phase changes from other variations (*e.g.,* input intensity fluctuations); even in a perfect measurement, it can be difficult to unambiguously extract $\Phi(t)$ from the detector signal. These shortcomings are largely addressed in the conventional and push-pull VISAR systems, which are constructed from multiple WAMI systems operating on different optical polarizations. In the former, a beam intensity monitor (BIM) is used to normalize the interferometer output signals, whereas the latter utilizes pairs of output signals that are subtracted from one another. In either case, the 2-4 detector signals are reduced to a pair of quadrature signals (D_x and D_y), which by virtue of a 1/8 wave plate in the interferometer are nearly 90° out of phase with one another. Unlike the WAMI, the quadrature signals of a VISAR system are largely insensitive to input intensity variations and incoherent light.

When plotted against one another, the quadrature signals from a VISAR map out an ellipse, where the angular position on the ellipse corresponds to a particular value of $\Phi(t)$. The

conversion of quadrature signals to phase difference is given by:

$$\tan\Phi = \tan\varepsilon + \frac{D_y - y_0\,A_x}{D_x - x_0\,A_y}\sec\varepsilon \qquad (6.2)$$

where x_0, y_0, A_x, A_y, and ε are the ellipse parameters for a particular VISAR system. Comparison of the phase difference at each moment in the experiment with an initial reference value yields the fringe shift $F(t)$.

$$F(t) = \frac{\Phi(t) - \Phi(t_i)}{2\pi} \qquad (6.3)$$

Since the tangent function is periodic, it is possible for $F(t)$ to be ambiguous within some integer shift.

6.2 Velocity calculation

The basic interpretation of a VISAR measurement is that changes in velocity correspond to changes in fringe shift. Fringe shift may be converted to mirror position by inverse analysis:

$$x(t) = x(t - \tau_0) + (1 + \delta)\tau_0 v_i + \frac{\lambda_0}{2}F(t) - \delta\tau_0 v(t - \tau_0) \qquad (6.4)$$

where τ_0 is the delay time of the interferometer at the operating wavelength λ_0, δ is a dispersion correction for the VISAR etalon, and v_i is the initial velocity of the mirror. This iterative calculation is conceptually straightforward, but the process is fraught with numerical difficulties and is only practical for low noise measurements.

In most situations, the VISAR approximation:

$$v(t) \approx v_i + K\,F(t) \qquad (6.5)$$

is more useful than inverse analysis. The parameter $K = \lambda_0/2(1 + \delta)\tau_0$ is known as the fringe constant, and is controlled by the size/construction of the VISAR system. The VISAR approximation neglects changes comparable to or faster than the interferometer delay time, which for many applications is reasonable. Better results, particularly for fast phenomena, are obtained from a time shifted version of the VISAR approximation:

$$v(t - \gamma\tau_0) \approx v_i + K\,F(t) \qquad (6.6)$$

where $\gamma \approx (1 + \delta)/2$. Events that occur faster than τ_0 are poorly resolved by the VISAR approximation and require inverse analysis.

6.3 Velocity corrections

Velocity corrections are required to account for conditions that alter the apparent velocity sensed by a VISAR. One class of velocity correction is the case of non-normal illumination

76

and/or reflection. Angular corrections are typically small ($\sim 0.1\%$) but may be important at extreme angles. In some cases, apparent velocity contains both longitudinal and transverse velocity information.

Another important class of velocity corrections occur whenever the VISAR measurement contains a compressed dielectric. In general, the calculation requires a great deal of information, but there are several special cases where the correction is straightforward. One special case involves materials compressed by a single shock wave, where the correction is a function of the refractive index ahead of and behind the front as well as the shock velocity. Another special case applies to materials where the refractive index is linear with density, leading to simple corrections regardless of the refractive index profile. Even in these simple cases, caution is required to deal with free surface motion.

6.4   Characterization and performance

The VISAR delay time is determined primarily by the physical length h and refractive index n of the etalon.

$$\tau = \frac{2h}{c_0}\left(n - \frac{1}{n}\right) \tag{6.7}$$

With careful interferometer construction and precise measurements of the etalon length, τ can be determined within 0.1%.

Etalon dispersion leads to a velocity dependent delay time:

$$\tau = \frac{2h}{c_0}\left[n - \frac{1}{n} - 2\lambda_0 \frac{dn}{d\lambda}\bigg|_{\lambda_0}\frac{v}{c_0}\right] = \tau_0\left(1 + 2\delta\frac{v}{c_0}\right) \tag{6.8}$$

where δ is on the order of several percent. In the VISAR approximation, the velocity dependence of τ cancels with other terms and leads to a constant correction to the fringe constant. For maximum precision, other components in the VISAR (*e.g.,* the beamsplitter) may be considered in the calculation of τ.

The five VISAR ellipse parameters x_0, y_0, A_x, A_y, and ε are required to accurately transform the measured quadrature signals into phase difference. Ideally, these parameters can be controlled during VISAR setup to achieve a circular ellipse, but the precise values must often be determined from ellipse fitting, parameter constraints, or some combination of the two techniques. Ellipse fitting uses quadrature signals (obtained either prior to or during a measurement) that map out the VISAR ellipse. The fitting process may be direct (which is fast, but has problems with incomplete data) or indirect (which is slow and may not converge, but can easily deal with constraints). Some ellipse parameters can be constrained to a desired value (*e.g.,* $x_0 = 0$) from characterization experiments prior to the VISAR experiment; this is particularly important for the push-pull VISAR configuration.

Contrast is a useful way to assess the performance of a VISAR system during a measurement. The dynamic contrast of a VISAR is a combination of the system contrast and the

optical signal that enters the interferometer, and is similar to the ellipse radius. Contrast loss is an indication of non-ideal behavior in a measurement. Sources of contrast loss include decreasing coherent light, increasing incoherent light, limited detector bandwidth, and multiphase interference.

The precision of a VISAR is limited by fringe ambiguity and fringe uncertainty. Fringe ambiguity arises from the periodicity in the tangent function—adding integer multiples of 2π to any phase difference yields the same quadrature signals. Such ambiguity can be eliminated by setting the fringe constant larger than the maximum expected velocity in a measurement. Physical insight and/or multiple VISAR measurements are alternative methods for dealing with fringe ambiguity. Fringe uncertainty arises from quadrature signal noise and imperfect characterization of the VISAR ellipse. The limiting resolution of a fringe shift measurement is approximately 0.001, and the practical resolution is 0.01-0.02. Fringe uncertainty can be mitigated by using small fringe constants where possible, although doing so may lead to fringe ambiguity.

References

[1] G.E. Duvall and R.A. Graham. Phase transitions under shock wave loading. *Reviews of Modern Physics*, 49(3):523, 1977.

[2] N.L. and Coleburn. Compressibility of pyrolytic graphite. *Journal of Chemical Physics*, 40(1):71, 1964.

[3] D.G. Doran. Hugoniot equation of state of pyrolytic graphite to 300 kbars. *Journal of Applied Physics*, 34(4):844, 1963.

[4] L.M. Barker and R.E. Hollenbach. Interferometer techniques for measuring the dynamic mechanical properties of materials. *Review of Scientific Instruments*, 36(11):1617, 1965.

[5] L.M. Barker and R.E. Hollenbach. Laser interferometer for measuring high velocities of any reflecting surface. *Journal of Applied Physics*, 43(11):4669, 1972.

[6] L.M. Barker. The development of the VISAR, and its use in shock compression science. In *Shock Compression of Condensed Matter–1999*, edited by M.D. Furnish (AIP Conference Proceedings v. 505, 2000), p. 11.

[7] B. Marshall. BN-STL fast push-pull VISAR, (U.S. patent pending).

[8] B. Marshall, 2005. BN-STL air delay VISAR, BN-STL-05-0022 (U.S. patent pending).

[9] D.H. Dolan, E. Kaltenbach, and K. McCollough. PointVISAR program (Sandia National Laboratories, Albuquerque, NM), 2005.

[10] C.F. McMillan, D.R. Goosman, N.L. Parker, L.L. Steinmetz, H.H. Chau, T. Huen, R.K. Whipkey, and S.J. Perry. Velocimetry of fast surfaces using Fabry-Perot interferometry. *Review of Scientific Instruments*, 59(1):1, 1988.

[11] O.T. Strand, L.V. Berzins, D.R. Goosman, W.W. Kuhlow, P.D. Sargis, and T.L. Whitworth. Velocimetry using heterodyne techniques. In *26th International Congress on High-Speed Photography and Photonics–2004*, edited by D.L. Paisley (Proc. SPIE v. 5580, 2005), p. 593.

[12] M. Born and E. Wolf. *Principles of Optics*. Cambridge University Press, Cambridge, 7th edition, 1999.

[13] A.A. Michelson. The relative motion of the earth and the luminiferous aether. *American Journal of Science*, 22:120, 1881.

[14] R.W. Boyd. *Radiometry and the detection of optical radiation*. John Wiler & Sons, New York, 1983.

[15] F.L. Pedrotti and L.S. Pedrotti. *Introduction to Optics*. Prentice-Hall, New Jersey, 2nd edition, 1987.

[16] J.D. Jackson. *Classical Electrodynamics*. John Wiley & Sons, New York, 2nd edition, 1975.

[17] W.H. Steel. *Interferometry*. Cambridge University Press, Cambridge, 1967.

[18] G. Hanson. *Z. Instrumentenk*, 61:411, 1941.

[19] E.G. Young and L.M. Barker. VISAR data reduction. Technical Report SAND-75-0424, Sandia National Laboratories, 1975.

[20] W.F. Hemsing. Velocity sensing interferometer (VISAR) modification. *Review of Scientific Instruments*, 50(1):73, 1979.

[21] P.A. Tipler. *Physics for scientists and engineers*. Worth Publishers, New York, 3rd edition, 1991.

[22] L.M. Barker. Laser interferometry in shock-wave research. *Experimental Mechanics*, 12(5):209, 1972.

[23] D.R. Goosman. Analysis of the laser velocity interferometer. *Journal of Applied Physics*, 46(8):3516, 1975.

[24] R.J. Clifton. Analysis of the laser velocity interferometer. *Journal of Applied Physics*, 41(13):5335, 1970.

[25] L.M. Barker. Velocity interferometer data reduction. *Review of Scientific Instruments*, 42(2):276, 1971.

[26] W.F. Hemsing. VISAR: displacement-mode data reduction. In *Ultrahigh- and High-Speed Photography, Videography, Photonics, and Velocimetry–1990*, edited by P. A. Jaanimagi (Proc. SPIE v. 1346, 1991), p. 141.

[27] L.M. Barker and R.E. Hollenbach. Shock-wave studies of PMMA, fused silica, and sapphire. *Journal of Applied Physics*, 41(10):4208, 1970.

[28] S.I. Grossman. *Calculus*. Harcourt Brace Jovanovich, San Diego, 4th edition, 1988.

[29] R.L. Burden and J.D. Faires. *Numerical Analysis*. PWS Publishing, Boston, 2nd edition, 1993.

[30] A. Savitzsky and M.J.E. Golay. Smoothing and differentiation of data by simplified least squares procedures. *Analytical Chemistry*, 36(8):1627, 1964.

[31] L.M. Barker. The accuracy of VISAR instrumentation. In *Shock Compression of Condensed Matter–1997*, edited by S.C. Schmidt (AIP Conference Proceedings v. 429, 1998), p. 833.

[32] W.C. Sweatt and O.B. Crump. Using a fast lens to collect the signal in a VISAR system. *Review of Scientific Instruments*, 6(12):2946, 1991.

[33] L.C. Chhabildas, H.J. Sutherland, and J.R. Asay. A velocity interferometer technique to determine shear-wave particle velocity in shock-loaded solids. *Journal of Applied Physics*, 50(8):5196, 1979.

[34] K.S. Kim, R.J. Clifton, and P. Kumar. A combined nomal- and transverse-displacement interferometer with an application to impact of y-cut quartz. *Journal of Applied Physics*, 48(10):4132, 1977.

[35] S.C. Jones and Y.M. Gupta. Refractive index and elastic properties of *z*-cut quartz shocked to 60 kbar. *Journal of Applied Physics*, 88(10):5671, 2000.

[36] L.M. Barker, V.J. Barker, and Z.B. Barker. VALYN VISARs user's handbook, 1999.

[37] R.E. Setchell. Refractive index of sapphire at 532 nm under shock compression and release. *Journal of Applied Physics*, 91(5):2833, 2002.

[38] S.C. Jones, M.C. Robinson, and Y.M. Gupta. Ordinary refractive index of sapphire in uniaxial tension and compression along the *c* axis. *Journal of Applied Physics*, 93(2):1023, 2003.

[39] D.B. Hayes, C.A. Hall, J.R. Asay, and M.D. Knudson. Continuous index of refraction measurements to 20 GPa in Z-cut sapphire. *Journal of Applied Physics*, 94(4):2331, 2003.

[40] S.C. Jones, B.A.M. Vaughan, and Y.M. Gupta. Refractive indices of sapphire under elastic, uniaxial strain compression along the *a* axis. *Journal of Applied Physics*, 90:4990, 2001.

[41] J.L. Wise and L.C. Chhabildas. Laser interferometer measurements of refractive index in shock-compressed materials. In *Shock Waves in Condensed Matter*, edited by Y.M. Gupta (4th APS Topical Conference, 1985), p. 441.

[42] J. Wackerle, H.L. Stacy, and J.C. Dallman. Refractive index effects for shocked windows in interface velocimetry. In *High Speed Photography, Videography, and Photonics V–1986*, edited by H.C. Johnson (Proc. SPIE v. 832, 1987), p. 72.

[43] D. Hayes. Unsteady compression waves in interferometry windows. *Journal of Applied Physics*, 89(11):6484, 2001.

[44] R.E. Setchell. Index of refraction of shock-compressed fused silica and sapphire. *Journal of Applied Physics*, 50(12):8186, 1979.

[45] M.D. Knudson et al. Principal Hugoniot, reverberating wave, and mechanical reshock measurements of liquid deuterium to 400 GPa using plate impact techniques. *Physical Review B*, 69(14):144209, 2004.

[46] L.M. Barker and K.W. Schuler. Correction to the velocity-per-fringe relationship for the VISAR interferometer. *Journal of Applied Physics*, 45(8):3692, 1974.

[47] P.L. Rosin. Assesing error of fit functions for ellipses. *Graphical Models and Image Processing*, 58(5):494, 1996.

[48] A.W. Fitzgibbon and R.B. Fisher. A buyer's guide to conic fitting. In *Proceedings of the 6th British conference on Machine vision*, (Birmingham, UK, v. 2, 1995), p. 513.

[49] W.H. Press, S.A. Teukolsky, W.T. Vetterling, and B.P. Flannery. *Numerical Recipies in C: The Art of Scientific Computing*. Cambridge University Press, New York, 2nd edition, 1992.

[50] A. Fitzgibbon, M. Pilu, and R.B. Fisher. Direct least square fitting of ellipses. *IEEE Transactions on Pattern Analysis and Machine Intelligence*, 21(5):476, 1999.

[51] R. Halíř and J. Flusser. Numerically stable direct least squares fitting of ellipses. In *Proc. 6th International Conference in Central Europe on Computer Graphics and Visualization. WSCG '98*, edited by V. Skala (University of West Bohemia Press, 1998), p. 125.

[52] J.R. Taylor. *An introduction to error analysis*. University Science Books, Sausalito, CA, 2nd edition, 1997.

[53] L. Veeser. VISAR detector study. BN-STL VISAR workshop, Santa Barbara, CA, Feb. 18-19, 2004 (unpublished).

[54] J.R. Asay and L.M. Barker. Interferometric measurement of shock-induced internal particle velocity and spatial variations of particle velocity. *Journal of Applied Physics*, 45(6):2540, 1974.

[55] D.R. Goosman, G.R. Avara, and S.J. Perry. Efficient optical probes for fast surface velocimetry: multiple frequency issues for Fabry and VISAR methods. In *24th International Congress on High-Speed Photography and Photonics–2000*, edited by K. Takayama (Proc. SPIE v. 4183, 2001), p. 413.

APPENDIX A

VISAR noise performance

The noise performance of a VISAR system can be quantified in terms of the noise impact Q, which is defined by the ratio of signal oscillation amplitude to noise amplitude.

$$Q \equiv \frac{\delta D}{A_D} \tag{A.1}$$

Since a push-pull VISAR [1] utilizes nearly twice as much of the coherent light as a comparable conventional VISAR [2], one expects the former to have half the noise impact of the latter. However, the precise noise benefit depends on the dominant noise mechanism. Two types of noise are considered here: photon limited and constant noise measurements.

Photon noise

Photon noise is the result of statistical fluctuations in photon flux [3]. These variations scale with the square root of the flux, and for a linear detector translate to the following signal noise:

$$\delta D = \gamma \sqrt{D} \tag{A.2}$$

where γ is a detector specific scaling factor.

For fixed input intensity, the signal output from one polarization of a conventional VISAR is simply a sinusoid centered on x_0 with an amplitude of Cx_0, where C is the system contrast (Section 2.3).

$$D_1 = x_0(1 + C \cos \Phi) \tag{A.3}$$

The signal undergoes random signal fluctuations δD_1, which can be determined from Equation A.2.

$$\delta D_1 = \gamma \sqrt{x_0(1 + C \cos \Phi)} \tag{A.4}$$

The noise impact of a conventional VISAR is thus as follows.

$$Q_c = \frac{\gamma}{C} \sqrt{\frac{1 + C \cos \Phi}{x_0}} \tag{A.5}$$

The same analysis can be applied a signal pair of a push-pull VISAR, which are assumed here to have the same mean and contrast.

$$D_{1A} = x_0(1 + C\cos\Phi) \quad D_{1B} = x_0(1 - C\cos\Phi)$$
$$D_1 = D_{1A} - D_{1B} = 2\,Cx_0\cos\Phi \tag{A.6}$$

If no additional noise is generated during signal subtraction, the total signal noise is simply the quadrature sum [4] of the signal noise from each detector.

$$(\delta D_1)^2 = (\delta D_{1A})^2 + (\delta D_{1B})^2 = 2\gamma^2 x_0 \tag{A.7}$$

The noise impact of a push-pull VISAR is thus a constant.

$$Q_{pp} = \frac{\gamma\sqrt{2x_0}}{2Cx_0} = \frac{\gamma}{C}\sqrt{\frac{1}{2x_0}} \tag{A.8}$$

The relative noise impact of each VISAR configuration can now be assessed by the ratio of Equation A.5 and Equation A.8.

$$q \equiv \frac{Q_c}{Q_{pp}} = \sqrt{2(1 + C\cos\Phi)} \tag{A.9}$$

When $q > 1$, the conventional configuration suffers from noise more than a comparable push-pull VISAR would; for $q < 1$, the push-pull configuration experiences greater noise problems. The limiting values of q are determined from the case of ideal contrast ($C = 1$).

$$\sqrt{2(1 - C)} \leq q \leq \sqrt{2(1 + C)} \tag{A.10}$$

The value of q is not always greater than unity—there are conditions where the conventional configuration outperforms the push-pull configuration.

One way of determining the better configuration is to calculate whether q is more likely to be above or below unity. From the symmetry of Equation A.9, the probability that $q > 1$ is given by:

$$P_{q>1} = \frac{\Phi_C}{\pi} \quad \text{where } 2(1 + \cos\Phi_C) = 1 \quad (\Phi_C \leq \pi) \tag{A.11}$$

which reduces to the following result.

$$P_{q>1} = \begin{cases} \dfrac{\arccos(-1/2C)}{\pi} & C > 1/2 \\ \\ 1 & \text{otherwise} \end{cases} \tag{A.12}$$

Since $P_{q>1} \geq 2/3$, one can conclude that the noise performance of a push-pull VISAR is generally better than a comparable conventional VISAR.

The next consideration is to quantify the average noise impact ratio over all possible phase differences (again using the symmetry of q).

$$\langle q \rangle = \frac{1}{\pi}\int_0^\pi \sqrt{2(1 + C\cos\Phi)}\,d\Phi \tag{A.13}$$

The limiting values of $\langle q \rangle$ may be determined analytically for $C = 0$ and $C = 1$.

$$\frac{4}{\pi} \leq \langle q \rangle \leq \sqrt{2} \tag{A.14}$$

For intermediate contrast values, Equation A.13 is an elliptic integral [5] that can be expressed as a (slowly converging) infinite sum:

$$\langle q \rangle = \sqrt{2}\left[1 - \left(\frac{1}{2\cdot 4}\right)\left(\frac{1}{2}\right)C^2 - \left(\frac{1\cdot 3\cdot 5}{2\cdot 4\cdot 6\cdot 8}\right)\left(\frac{1\cdot 3}{2\cdot 4}\right)C^4 - \ldots\right] \tag{A.15}$$

or evaluated numerically. The results shown in Figure A.1 indicate that noise in a conventional VISAR will have roughly 40% higher impact than in a push-pull VISAR.

An additional consideration in comparing the two VISAR configurations is the fact that signal noise does not directly couple to phase difference uncertainty—some ellipse positions are more sensitive than others to signals noise (Section 5.4.2). Strictly speaking, Equation A.13 should be weighted by $\partial\Phi/\partial x$. As a quick approximation, consider the noise performance ratio where it matters most ($\Phi = \pi/2$ and $3\pi/2$). At those locations, $q = \sqrt{2}$, which is consistent with the value of $\langle q \rangle$.

Fixed amplitude noise

Signal noise may not be dominated by statistical variations of photon flux. For example, thermal noise will be present in all detectors not operating at absolute zero; digitizing systems also add to the signal noise. Unlike photon noise, these fluctuations need not scale with the intensity striking the detector, but are instead related to the detection/acquisition system. For simplicity, all non-photon noise will be combined into a constant total signal noise δD.

In a conventional VISAR, constant signal noise leads to a constant noise impact.

$$Q_c = \frac{\delta D_1}{Cx_0} \tag{A.16}$$

Similar noise would occur in each detector pair of a push-pull VISAR.
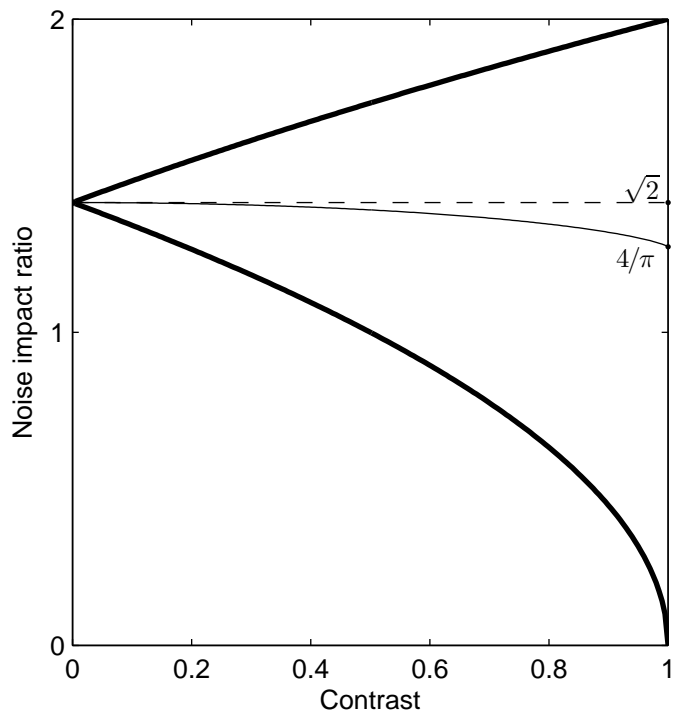
$$(\delta D_1)^2 = (\delta D_{1A})^2 + (\delta D_{1B})^2 \approx 2(\delta D_{1A})^2 \tag{A.17}$$

$$Q_{pp} = \frac{\sqrt{2}\delta D_{1A}}{2Cx_0} \tag{A.18}$$

The noise impact ratio is thus constant:

$$q = \frac{\rho_c}{\rho_{pp}} = \sqrt{2} \tag{A.19}$$

indicating once again that noise has approximately 40% greater impact in a conventional VISAR than a push-pull VISAR.

Figure A.1. Noise impact ratio as a function of contrast
The average noise impact ratio (conventional/push-pull VISAR)
varies between $\sqrt{2}$ and $4/\pi$, depending on contrast. For refer-
ence, the upper and lower limits of this ratio are also shown (heavy
lines).

Summary

Regardless of the type of limiting noise in a VISAR measurement, a push-pull VISAR *should* provide a lower noise impact than a conventional VISAR. However, the theoretical enhancement is of order $\sqrt{2}$, not 2. Note that the actual performance of a push-pull VISAR will be reduced when noise is generated during the subtraction process, *i.e.* in the differential amplifier (if present).

References

[1] W.F. Hemsing. Velocity sensing interferometer (VISAR) modification. *Review of Scientific Instruments*, 50(1):73, 1979.

[2] L.M. Barker and R.E. Hollenbach. Laser interferometer for measuring high velocities of any reflecting surface. *Journal of Applied Physics*, 43(11):4669, 1972.

[3] R.W. Boyd. *Radiometry and the detection of optical radiation*. John Wiler & Sons, New York, 1983.

[4] J.R. Taylor. *An introduction to error analysis*. University Science Books, Sausalito, CA, 2nd edition, 1997.

[5] G.B. Arkfen and H.J. Weber. *Mathematical Methods for Physicists*. Academic Press, San Diego, 4th edition, 1995.

DISTRIBUTION:

2 T.J. Ahrens
Division of Geological and Planetary Sciences
California Institute of Technology
MC 170-25
Pasadena, CA 91125

1 L.M. Barker
3926 Simms S.E.
Albuquerque, NM 87108

2 R.J. Clifton
Department of Engineering
Brown University
Providence, RI 02912

2 J. Forbes
University of Maryland
6535 Chelsea Way
Port Tobacco, MD 20677

5 Y.M. Gupta
Institute for Shock Physics
Washington State University
Pullman, WA 99164-2816

1 D.B. Hayes
P.O. Box 591
Tijeras, NM 8759

3 R.J. Hemley
Carnegie DOE Alliance Center
5251 Broad Branch Road, NW
Washington DC 20015-1305

2 R. Jeanloz
Department of Earth and Planetary Sciences
University of California, Berkeley
491 McCone
Berkeley, CA 94720-4767

2 W.J. Nellis
Department of Physics
Harvard University
Cambridge, MA 02138

2 M.F. Nicol
UNLV High Pressure Sciences and Engineering Center
University of Nevada, Las Vegas
Box 454002
4505 South Maryland Parkway
Las Vegas, NV 89154-4002

2 S.T. Stewart-Mukhopadhyay
Department of Earth and Planetary Sciences
Harvard University
20 Oxford Street
Cambridge MA 02138

2 N.N. Thadhani
Materials Science and Engineering
Georgia Institute of Technology
771 Ferst Drive, N.W.
Atlanta, GA 30332-0245

2 US Army Research Laboratory
AMSRL-WM-TD
Aberdeen Proving Ground, MD 21005-5069
  Attn: D. Dandekar

4 Applied Research Associates, Inc.
4300 San Mateo Blvd. NE
Suite A-200
Albuquerque, NM 87110
  Attn: C. Doolittle
          D.E. Grady
          E. Kaltenbach
          K. McCollough

5 Bechtel Nevada
Los Alamos Operations
P.O. Box 809
Los Alamos, NM 87544
  Attn: D. Esquibel
          C. Gallegos
          A. Iverson
          V. Romero
          R. Yeh

4   Bechtel Nevada
Las Vegas Operations
PO Box 98521
Las Vegas, NV 89193
  Attn: D. Barker
             S.A. Becker
             E. Daykin
             S. Goldstein

4   Bechtel Nevada
Special Technologies Laboratory
5520 "B" Ekwill Street
Santa Barbara, CA 93111
  Attn: B. Marshall
             G. Stevens
             W.D. Turley
             L. Veeser

2   Naval Surface Warfare Center
101 Strauss Avenue
Indian Head, MD 20640
  Attn: J.M. Boteler
             G. Sutherland

13 Lawrence Livermore National Laboratory
7000 East Ave.
Livermore, CA 94550
  Attn: M. Bastea
             R. Chau
             G.W. Collins
             J.H. Eggert
             D.J. Erskine
             D.R. Goosman
             N.C. Holmes
             J.O. Kane
             J.H. Nguyen
             D.B. Reisman
             B.A. Remington
             K.S. Vandersall
             C.S. Yoo

18 Los Alamos National Laboratory
P.O. Box 1663
Los Alamos, NM 87545
  Attn: W. Anderson
             M. Briggs
             D.M. Dattelbaum
             D. Dennis-Koller
             R.L. Gustavsen
             W. Hemsing
             R.S. Hixson
             D. Holtkamp
             B.J. Jensen
             A.W. Obst
             D.L. Paisley
             P.A. Rigg
             D.L. Robbins
             S. Sheffield
             D.C. Swift
             D.G. Tasker
             T.E. Tierney
             M.D. Wilke

1   MS 1181
S.C. Alexander, 1647

1   MS 1181
T. Ao, 1646

1   MS 1181
J.R. Asay, 1646

1   MS 1194
D.E. Bliss, 1644

2   MS 1181
L.C. Chhabildas, 1647

1   MS 1181
J.-P. Davis, 1646

2   MS 1181
C. Deeney, 1646

20 MS 1181
D.H. Dolan, 1646

1   MS   1181
    M.D. Furnish, 1647

2   MS   1181
    C.A. Hall, 1646

1   MS   1181
    R.J. Hickman, 1646

1   MS   1159
    S.C. Jones, 1344

1   MS   1181
    M.D. Knudson, 1646

1   MS   1181
    B.R. McWatters, 1646

1   MS   1181
    M.D. Roderick, 1646

1   MS   1181
    J.W. Podsednik, 1646

1   MS   1181
    W.D. Reinhart, 1647

1   MS   1421
    R.E. Setchell, 1111

1   MS   1181
    T.F. Thornhill, 1647

1   MS   0834
    W.M. Trott, 9112

1   MS   1181
    T.J. Vogler, 1647

1   MS   1181
    J.L. Wise, 1646

2   MS   9018
    Central Technical Files, 8944

2   MS   0899
    Technical Library, 4536